

Beyond Limber: Efficient computation of angular power spectra for galaxy clustering and weak lensing

Xiao Fang,¹ Elisabeth Krause,^{1,2} Tim Eifler,¹ and Niall MacCrann^{3,4}

¹Department of Astronomy and Steward Observatory, University of Arizona, 933 N Cherry Ave, Tucson, AZ 85719

²Department of Physics, University of Arizona, 1118 E Fourth Str, AZ 85721

³Center for Cosmology and Astro-Particle Physics, The Ohio State University, Columbus, OH 43210, USA

⁴Department of Physics, The Ohio State University, Columbus, OH 43210, USA

E-mail: xfang@email.arizona.edu

Abstract. Angular two-point statistics of large-scale structure observables are important cosmological probes. To reach the high accuracy required by the statistical precision of future surveys, some of these statistics may need to be computed without the commonly employed Limber approximation; the exact computation however requires integration over Bessel functions, and a brute-force evaluation is slow to converge. We present a new method based on our generalized FFTLog algorithm for the efficient computation of angular power spectra beyond the Limber approximation. The new method significantly simplifies the calculation and improves the numerical speed and stability. It is easily extended to handle integrals involving derivatives of Bessel functions, making it equally applicable to numerically more challenging cases such as contributions from redshift-space distortions and Doppler effects. We implement our method for galaxy clustering and galaxy-galaxy lensing power spectra. We find that using the Limber approximation for galaxy clustering in future analyses like LSST Year 1 and DES Year 6 may cause significant biases in cosmological parameters, indicating that going beyond the Limber approximation is necessary for these analyses.

Keywords: cosmological parameters from LSS, dark energy experiments, galaxy clustering, weak gravitational lensing

Contents

1	Introduction	1
2	Non-Limber Angular Power Spectra	3
2.1	Example: Galaxy Clustering	4
2.2	Reduction to 1D Bessel Integrals	5
2.2.1	Accuracy of Limber Approximation for Separable Power Spectra	6
2.2.2	Approximations for Scale-Dependent Growth	7
3	FFTLog and Beyond	8
3.1	Review of FFTLog	8
3.2	Beyond FFTLog	9
4	Applications	10
4.1	Galaxy Clustering Power Spectrum	10
4.2	Galaxy-Galaxy Lensing Power Spectrum	12
5	Significance for Future Survey Analyses	13
5.1	Analysis Ingredients	13
5.1.1	Lens and Source Galaxy Sample Distributions	13
5.1.2	Angular Two-Point Functions	15
5.1.3	Systematics	16
5.1.4	Covariances	18
5.1.5	Angular Scale Cuts	18
5.2	Simulated Likelihood Analysis	19
5.2.1	The Impact of Limber Approximation	19
5.2.2	The Impact of n_s Priors	20
6	Discussion and Summary	21
A	Useful Identities	23
B	FFTLog Versus Brute-Force	23

1 Introduction

Current and future photometric surveys, such as KiDS¹, HSC², DES³, LSST⁴, WFIRST⁵, SPHEREx⁶, aim to measure the structure of the late-time Universe at high accuracy, enabling precise analyses of various correlations of tracers (galaxy density, weak lensing, galaxy clusters,

¹Kilo-Degree Survey, <http://kids.strw.leidenuniv.nl/>

²Hyper Suprime-Cam, <https://www.naoj.org/Projects/HSC/>

³Dark Energy Survey, <https://www.darkenergysurvey.org>

⁴Large Synoptic Survey Telescope, <https://www.lsst.org/>

⁵Wide Field Infrared Survey Telescope, <https://wfirst.gsfc.nasa.gov/>

⁶Spectro-Photometer for the History of the Universe, Epoch of Reionization, and Ices Explorer, <http://spherex.caltech.edu/>

etc.). Ultimately these endeavors will provide powerful constraints on the nature of dark energy and tests of theories of gravity on cosmological scales. Analyses of photometric surveys primarily use the angular two-point statistics as cosmological probes. The so-called “ $3 \times 2\text{pt}$ ” analysis, combining the galaxy clustering, the galaxy-galaxy lensing (GGL), and the lensing shear-shear correlation, has become a standard set of probes in DES and part of the baseline analysis of LSST-DESC [1], while joint analyses with other probes e.g., CMB anisotropies and lensing, cluster clustering and lensing, etc., are also playing important roles or currently being investigated.

The modeling of the angular power spectra of two tracers involves double (spherical) Bessel integrals or their derivatives in the form of ⁷

$$\int d\chi_1 w_1(\chi_1) \int d\chi_2 w_2(\chi_2) \int_0^\infty dk f(k, z(\chi_1), z(\chi_2)) j_\ell^{(n_1)}(k\chi_1) j_\ell^{(n_2)}(k\chi_2), \quad (1.1)$$

where n_1, n_2 are the orders of the derivatives, χ_1, χ_2 are the comoving distances, $w_1(\chi_1), w_2(\chi_2)$ are the tracers’ selection functions (characterizing the efficiency of observing the tracers or their relevant quantities as functions of redshifts), and $f(k, z(\chi_1), z(\chi_2))$ is a smooth function of the wavenumber k and two tracers’ redshifts. The full calculation can be numerically challenging due to the rapidly oscillatory nature of the Bessel functions. The Limber approximation [3–5] simplifies the integrals by approximating the spherical Bessel function as a Dirac delta function located at its first peak, i.e., $j_\ell(x) \simeq \sqrt{\pi/(2\ell+1)}\delta(\ell+1/2-x)$ [e.g., 6, 7]. The derivatives of the spherical Bessel functions can be written in terms of a few spherical Bessel functions of different orders using the recurrence relations, and then approximated with Delta functions. However, this approximation only works well when (1) the (smooth) selection function has a radial width $\Delta\chi$ much larger than the scales of the tracer’s fluctuation modes that we are probing (i.e., $\Delta\chi \gg 1/k \sim \bar{\chi}/\ell$, where $\bar{\chi}$ is the mean distance), and (2) the two selection functions largely overlap in redshift, and (3) $\ell \gg 1$ (see e.g., [8, 9] for more discussions). The first requirement is violated, for example, when the photometric redshifts are sufficiently accurate for galaxy clustering measurements and the tomographic bins are chosen so narrow that the selection function is too narrow. The second requirement is violated, for example, when cross correlating different narrow tomographic bins of galaxy density fields. The third requirement is violated, for example, when modeling wide-angle correlations.

The Limber approximation may not be sufficient for modeling angular two-point statistics in analyses of upcoming surveys for several reasons: (1) The aforementioned requirements are violated when the analyses employ narrower tomography bins enabled by the improved photometric redshift accuracy, or when wide-angle correlations are modeled; (2) the improved constraining power can no longer tolerate the errors introduced by the approximation. One may extend the Limber approximation by including high-order correction terms in the series expansion of the angular power spectra in $1/(\ell+1/2)$, as suggested in [9]. However, its accuracy will still depend on the value of ℓ , and the widths, shapes, and mean redshifts of the selection functions. Meanwhile, including higher-order terms does not alleviate the divergence of the series expansion at small ℓ , and the convergence radius is case-dependent.

Several approaches have been developed to efficiently evaluate the double Bessel integral in Eq. (1.1), and Fast Fourier Transform (FFT) techniques usually play a central role. In general, the FFT-based methods perform a power-law decomposition of the smooth part of the

⁷This form only works for flat cosmologies. For curved cosmologies, the functional forms of f and w_1, w_2 are modified, and the spherical Bessel functions are replaced with the hyperspherical Bessel functions (see e.g., [2]).

integrand, each component integral is then calculated analytically, and finally a re-summation of the components yields the result. This approach derives from the FFTLog algorithm, which has long been used to efficiently evaluate single Bessel or spherical Bessel integrals. In Ref. [10–12], the “1D-FFTLog” method is developed, which decomposes the double Bessel integral into a series of power-law double Bessel integrals (i.e., $\int_0^\infty dk k^\alpha j_\ell(kr_1)j_\ell(kr_2)$), each of which has an analytic solution in terms of Gamma functions and hypergeometric functions. However, the evaluations of hypergeometric functions can be numerically challenging, and require specialized methods to improve the speed and stability [11]. In addition, FFTLog based algorithms have also been used to accelerate the computation of the one-loop and two-loop order nonlinear perturbation theories in cosmology [e.g., 13–19]. AngPow [20] takes a different approach and optimizes the quadrature integration by using a Clenshaw-Curtis-Chebyshev algorithm and significantly reducing the number of the sampled values, leading to similar or faster computation depending on the properties of the integrands and the sampling points.

In this paper, we present a novel FFTLog based method for solving the non-Limber integrals. Instead of speeding up the double-Bessel integrals, we simplify the full non-Limber angular power spectrum integral by noting the small contribution from unequal-time nonlinear terms, which leads to a significant reduction of the computation and avoiding the double-Bessel integral. We also extend the original FFTLog algorithm to be able to compute integrals containing derivatives of Bessel functions, which can be used to efficiently compute angular power spectra including redshift-space distortions (RSD) and Doppler effects.

This paper is structured as follows. In §2, we start with the example of galaxy clustering and introduce our approximation for simplifying the integrals. We show that with this approximation the power spectrum reduces to integrals containing a single Bessel function or its derivative. In §3, we review the FFTLog algorithm for single-Bessel integrals and generalize it for integrals containing a derivative of the Bessel function. In §4, we apply our method to two types of angular power spectra: galaxy clustering and GGL, and compare our FFTLog results with the traditional quadrature integration (hereafter “brute-force”) results. In §5, we investigate the significance of including non-Limber galaxy clustering and GGL power spectra in future survey analyses such as DES Year 6 (DES Y6) and LSST Year 1 (LSST Y1). Finally, we discuss other applications and summarize in §6. Some useful special function identities are provided in Appendix A. We show more FFTLog and brute-force comparison results in Appendix B.

2 Non-Limber Angular Power Spectra

In the linear regime, the angular power spectrum between tracers a at redshift z_1 and b at redshift z_2 can be written as

$$C_\ell^{ab} = \frac{2}{\pi} \int_0^\infty \frac{dk}{k} k^3 P_\Phi(k) \Delta_\ell^a(k, z_1) \Delta_\ell^b(k, z_2), \quad (2.1)$$

where $P_\Phi(k)$ is the power spectrum of the primordial curvature perturbations, and Δ^a and Δ^b are the transfer functions of the tracers (see e.g., Section 2.4.1 of [7] for a list of examples), each of which contains a spherical Bessel integral or its derivative. On small scales (large ℓ), the Limber approximation can be applied to reduce the integral.

In §2.1 we use galaxy clustering as an example to illustrate the problem. In §2.2, we introduce a method to significantly simplify the problem, avoiding the trouble of computing double Bessel integrals.

2.1 Example: Galaxy Clustering

Galaxy clustering quantifies correlations between galaxy number density fields (we will focus on auto-correlations in this work). From now on we assume a linear galaxy bias model⁸, but comment on the application to non-linear bias models at the end of §2.2. The galaxy number density transfer function Δ^g has 3 components: a galaxy density contribution Δ^D that is proportional to the dark matter density, a linear contribution from redshift space distortions (RSD) Δ^{RSD} , and a lensing magnification contribution Δ^M . Following [7] and putting back the speed of light constant c , they are given by

$$\Delta_\ell^D = \int dz n_z(z) b(z) T_\delta(k, z) j_\ell(k\chi(z)) , \quad (2.2)$$

$$\Delta_\ell^{\text{RSD}}(k) = \int dz \frac{(1+z)n_z(z)}{H(z)} T_\theta(k, z) j_\ell''(k\chi(z)) , \quad (2.3)$$

$$\Delta_\ell^M(k) = -\ell(\ell+1) \int \frac{dz}{cH(z)} W^M(z) T_{\phi+\psi}(k, z) j_\ell(k\chi(z)) , \quad (2.4)$$

where z is redshift, n_z is the normalized redshift distribution of the galaxies, b is the galaxy linear clustering bias, $T_\delta, T_\theta, T_{\phi+\psi}$ are the transfer function of matter perturbations δ , velocity divergences θ , and the Newtonian-gauge scalar metric perturbations, respectively, and are related to each other by

$$T_\theta(k, z) = -\frac{H(z)f(z)}{1+z} T_\delta(k, z) , \quad T_{\phi+\psi}(k, z) = -\frac{3H_0^2\Omega_m(1+z)}{k^2} T_\delta(k, z) . \quad (2.5)$$

χ is the comoving distance, H is the Hubble parameter, Ω_m is the matter density fraction at present, and W^M is the lensing magnification window function, given by

$$W^M(z) = \int_z^\infty dz' n_z(z') \frac{b_{\text{mag}}(z')}{2} \frac{\chi(z') - \chi(z)}{\chi(z)\chi(z')} , \quad (2.6)$$

where b_{mag} is the magnification bias parameter which encapsulates the linear dependence of the galaxy number density on the convergence at a given point on the sky⁹ (due to the change in solid angle and e.g., luminosity cuts [21–23] and size cuts [24, 25]). The angular power spectrum of galaxy number counts is thus

$$C_\ell^{\text{gg}} = \frac{2}{\pi} \int_0^\infty \frac{dk}{k} k^3 P_\Phi(k) \Delta_\ell^g(k, z_1) \Delta_\ell^g(k, z_2) , \quad (2.7)$$

where $\Delta_\ell^g = \Delta_\ell^D + \Delta_\ell^{\text{RSD}} + \Delta_\ell^M$.

The expansion of the product of Δ_ℓ^g 's leads to integrals containing two Bessel functions and their derivatives. For example, the ‘‘DD’’ component is

$$C_\ell^{\text{DD}} = \frac{2}{\pi} \int dz_1 n_z(z_1) b(z_1) \int dz_2 n_z(z_2) b(z_2) \int_0^\infty \frac{dk}{k} k^3 P_\delta(k, z_1, z_2) j_\ell(k\chi(z_1)) j_\ell(k\chi(z_2)) , \quad (2.8)$$

⁸The linear galaxy bias model assumes the galaxy power spectrum is proportional to the matter power spectrum. Here we use the nonlinear matter power spectrum rather than the linear power spectrum.

⁹defined such that the galaxy overdensity δ_g is changed by $\Delta\delta_g = b_{\text{mag}}\kappa\delta_g$, where κ is the lensing convergence.

where $P_\delta(k, z_1, z_2) = P_\Phi(k)T_\delta(k, z_1)T_\delta(k, z_2)$ is the matter power spectrum across two redshifts z_1, z_2 , while projected power spectra involving the RSD have integrands containing $j_\ell j_\ell''$ or $j_\ell'' j_\ell''$. A brute-force way of computing the non-Limber angular power spectra is to calculate the “double Bessel” integrals for a grid of (z_1, z_2) and then perform the outer z_1 and z_2 integrals. Quadrature integration is known to be slow and numerically unstable due to the rapid oscillations of, and the beatings between, the spherical Bessel functions. Various efficient algorithms have been developed for the double Bessel integrals containing $j_\ell j_\ell$, as described in §1. An efficient algorithm for $j_\ell j_\ell''$ or $j_\ell'' j_\ell''$ has been discussed in Ref. [12], where integration by parts is used to move the derivative operator from the Bessel functions to the smooth part of the integrand.

2.2 Reduction to 1D Bessel Integrals

We now describe a generic and efficient method to calculate the non-Limber integrals without the aforementioned FFTLog methods for double-Bessel integrals.

This method requires the redshift dependence of the matter power spectrum in the non-Limber integral to factorize, hence we adopt a separation of the linear part $P_{\text{lin}}(k, z_1, z_2)$ and nonlinear contribution $(P_\delta - P_{\text{lin}})(k, z_1, z_2)$ of the power spectrum. The redshift evolution of the linear part is simply a scaling by the growth factor $G(z)$, i.e.,

$$P_{\text{lin}}(k, z_1, z_2) = P_{\text{lin}}(k, 0)G(z_1)G(z_2), \quad (2.9)$$

where $P_{\text{lin}}(k, 0) = P_{\text{lin}}(k, z = 0)$ is the linear matter power spectrum at present (we will comment at the end of this subsection on scale dependent growth).

The nonlinear contribution is significant only on small scales where the Limber approximation is sufficiently accurate, as we demonstrate later in this subsection. This separation avoids the computation of the unequal-time nonlinear power spectrum $P_\delta(k, z_1, z_2)$ (e.g., [26, 27]). Applying this separation to the example of C_ℓ^{DD} and with the monotonic function $\chi(z)$, we can rewrite Eq. (2.8) as

$$\begin{aligned} C_\ell^{\text{DD}} &= \frac{2}{2\ell + 1} \int_0^\infty dk [\tilde{\Delta}^{\text{D}}(\chi_\ell)]^2 [P_\delta(k, z(\chi_\ell)) - P_{\text{lin}}(k, z(\chi_\ell))] \\ &\quad + \frac{2}{\pi} \int d\chi_1 \tilde{\Delta}^{\text{D}}(\chi_1) G(z(\chi_1)) \int d\chi_2 \tilde{\Delta}^{\text{D}}(\chi_2) G(z(\chi_2)) \int_0^\infty \frac{dk}{k} k^3 P_{\text{lin}}(k, 0) j_\ell(k\chi_1) j_\ell(k\chi_2), \end{aligned} \quad (2.10)$$

where $\tilde{\Delta}^{\text{D}}(\chi) = \frac{1}{c} n_z(z(\chi)) b(z(\chi)) H(z(\chi))$ and $\chi_\ell = (\ell + 1/2)/k$. Now we can avoid computing the double-Bessel integral by switching the order of integration in the second term, i.e.,

$$\frac{2}{\pi} \int_0^\infty \frac{dk}{k} k^3 P_{\text{lin}}(k, 0) \left[\int \frac{d\chi_1}{\chi_1} \chi_1 \tilde{\Delta}^{\text{D}}(\chi_1) G(z(\chi_1)) j_\ell(k\chi_1) \right] \left[\int \frac{d\chi_2}{\chi_2} \chi_2 \tilde{\Delta}^{\text{D}}(\chi_2) G(z(\chi_2)) j_\ell(k\chi_2) \right]. \quad (2.11)$$

The two integrals in the square brackets are Hankel transforms that can be efficiently calculated with the original FFTLog algorithm. The outer k integral can be computed with quadrature integration. In total, this method involves four FFTs (each Hankel transform takes 1 FFT to get Fourier coefficients and 1 FFT to sum up, $\mathcal{O}(N \log N)$, see §3.1) and one quadrature ($\mathcal{O}(N)$).

For correlations involving RSD, we obtain integrals in the form of Eq. (2.11) except that either or both of the spherical Bessel functions are replaced by their second derivatives, where a modified FFTLog algorithm is needed, which will be introduced in §3.

The Limber approximation of the nonlinear correction term ($P_\delta - P_{\text{lin}}$) in Eq. (2.10) is sufficiently accurate in realistic cases. Assuming the nonlinear contribution is important for Fourier modes $k \geq k_{\text{cr}}$, these modes are projected onto the sky and mostly contribute to angular modes $\ell \simeq k\bar{\chi} \geq k_{\text{cr}}\bar{\chi}$, where $\bar{\chi}$ is the mean comoving distance of the selection function. In the case of auto-correlation, based on our discussion in §1 and [9], the Limber approximation is accurate if $\ell \gg \bar{\chi}/\Delta\chi$, where $\Delta\chi$ is the width of the selection function. Thus, as long as $k_{\text{cr}} \gg 1/\Delta\chi$, it is safe to apply the Limber approximation to the nonlinear contribution¹⁰. For example, for a narrow tomographic bin centered at $\bar{\chi} = 2000$ Mpc (redshift ~ 0.5), with a redshift width $\Delta z = 0.2$, i.e., a distance width $\Delta\chi \sim 660$ Mpc, the criterion becomes $k_{\text{cr}} \gg 1.5 \times 10^{-3} \text{ Mpc}^{-1}$. The fractional difference between P_δ and P_{lin} is well within 1% for $k < 0.01h/\text{Mpc}$ and within $\sim 5\%$ for $k < 0.2h/\text{Mpc}$, implying that the criterion $k_{\text{cr}} \gg 1/\Delta\chi_{\text{max}}$ is well satisfied in realistic cases.

We test the approximation quantitatively in §2.2.1, and extend our algorithm to the scale-dependent growth in §2.2.2.

2.2.1 Accuracy of Limber Approximation for Separable Power Spectra

The Limber approximation only picks up the contributions from the equal-time matter power spectra. To assess the impact of the unequal-time nonlinear matter power spectrum $P_\delta(k, z_1, z_2)$, we define a ‘‘scaled’’ nonlinear matter power spectrum $P_\delta^{(\text{scaled})}(k, z_1, z_2)$ which follows the linear growth scaling $P_\delta^{(\text{scaled})}(k, z_1, z_2) = P_\delta(k, 0)G(z_1)G(z_2)$, where $P_\delta(k, 0) = P_\delta(k, z = 0)$. Similar to Eq. (2.10), we can split C_ℓ^{DD} into two parts and use the Limber approximation on the first term, i.e.

$$C_\ell^{\text{DD}} = \frac{2}{2\ell + 1} \int_0^\infty dk [\tilde{\Delta}^{\text{D}}(\chi_\ell)]^2 [P_\delta(k, z(\chi_\ell)) - P_\delta(k, 0)(G(z(\chi_\ell)))^2] \\ + \frac{2}{\pi} \int d\chi_1 \tilde{\Delta}^{\text{D}}(\chi_1)G(z(\chi_1)) \int d\chi_2 \tilde{\Delta}^{\text{D}}(\chi_2)G(z(\chi_2)) \int_0^\infty \frac{dk}{k} k^3 P_\delta(k, 0) j_\ell(k\chi_1) j_\ell(k\chi_2), \quad (2.12)$$

We denote the C_ℓ^{DD} from this alternative splitting as C_ℓ^{scaled} .

Since $P_\delta^{(\text{scaled})}(k, z_1, z_2) > P_\delta(k, z_1, z_2) > P_{\text{lin}}(k, z_1, z_2)$ for any redshift $z_1, z_2 > 0$,¹¹ C_ℓ^{scaled} overestimates the unequal-time nonlinear contribution from the matter power spectrum. Thus, the fractional difference ϵ_ℓ between C_ℓ^{DD} in Eq. (2.10) and C_ℓ^{scaled} , i.e., $\epsilon_\ell = |C_\ell^{\text{DD}}/C_\ell^{\text{scaled}} - 1|$, provides an upper-bound on the error from using the Limber approximation for $(P_\delta - P_{\text{lin}})(k, z_1, z_2)$.

In Figure (1), we show in solid lines the fractional differences ϵ_ℓ between C_ℓ^{DD} and C_ℓ^{scaled} for $\ell \leq 50$ and for the 5 lens tomographic bins of LSST Y1 described in §5.1.1, and find the errors are all below $\sim 0.35\%$. We also plot in dashed lines the fractional differences between Eq. (2.10) and the full Limber version of C_ℓ^{DD} , showing that using the Limber approximation of C_ℓ^{DD} results in a $\sim 1\%$ error up to $\ell = 50$.

¹⁰For two bins peaked at unequal $\bar{\chi}_1, \bar{\chi}_2$ with comoving radial widths $\Delta\chi_1 = \Delta\chi_2$, the criterion (see [9]) becomes $k_{\text{cr}} \gg |\bar{\chi}_1 - \bar{\chi}_2|/(\Delta\chi_1\Delta\chi_2)$.

¹¹This is true for the geometric approximation, $P_\delta(k, z_1, z_2) \simeq \sqrt{P_\delta(k, z_1)P_\delta(k, z_2)}$, and we have verified for the HALOFIT and SPT 1-loop nonlinear power spectrum. For $z_1 \neq z_2$, with the more accurate Zel’dovich approximation, $P_\delta(k, z_1, z_2)$ cuts off exponentially at $k \gtrsim k_{\text{NL}}/|G(z_1) - G(z_2)|$ [27], where the nonlinear scale is defined as $k_{\text{NL}}^{-2} = (12\pi^2)^{-1} \int_0^\infty P_{\text{lin}}(k') dk'$. The cut-off, effective at large k (typically $\gg 0.1h/\text{Mpc}$), suppresses the unequal-time contributions, hence improving the accuracy of the Limber approximation.

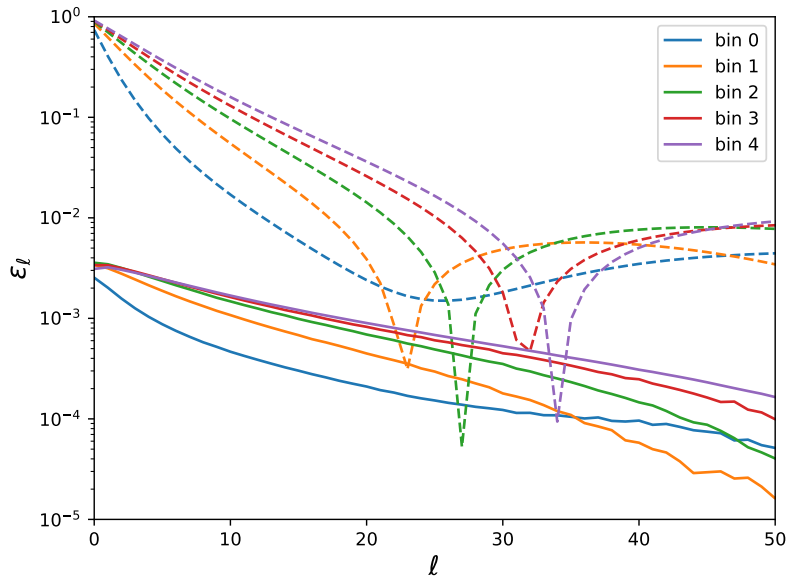


Figure 1. The solid lines show the fractional differences ϵ_ℓ between C_ℓ^{DD} in Eq. (2.10) and C_ℓ^{scaled} in Eq. (2.12) for the 5 lens tomographic bins of LSST Y1 described in §5.1.1. Bins 0-5 are ordered with increasing redshifts. C_ℓ^{scaled} overestimates the unequal-time nonlinear contribution from the matter power spectrum. Thus, ϵ_ℓ is an over-estimation of the impact of the Limber approximation of the first term in Eq. (2.10). We also plot in dashed lines the fractional differences between Eq. (2.10) and the full Limber version of C_ℓ^{DD} .

The high accuracy of the Limber approximation for the nonlinear contribution also suggests that a similar split can be applied to perturbative galaxy clustering power spectra, where the non-Limber integral is then carried out over the leading order term, and higher-order terms contribute only in the Limber approximation.

2.2.2 Approximations for Scale-Dependent Growth

The separability of the redshift-dependence in the linear power spectrum fails when the growth is scale dependent e.g., when there are massive neutrinos. However, for the case where the Limber approximation breaks due to narrow tomographic bins, the scale-dependent contribution to the growth should be small within each bin, and our method can be extended to this case. After performing the linear and nonlinear power spectrum separation as in §2.2, we again apply the Limber approximation for the nonlinear correction part, while the linear part is inseparable. We define scale-dependent growth factor as $G(k, z) = \sqrt{P_{\text{lin}}(k, z)/P_{\text{lin}}(k, 0)}$. Thus, the equal-time linear power spectrum at redshift z within some narrow bin with a mean value \bar{z} is given by

$$P_{\text{lin}}(k, z) = P_{\text{lin}}(k, \bar{z}) [G(k, z)/G(k, \bar{z})]^2 \simeq P_{\text{lin}}(k, \bar{z}) [g_{\text{eff}}(z, \bar{z})]^2, \quad (2.13)$$

where in the second step we neglect the scale-dependent growth within the narrow redshift bin and approximate the growth factor ratio as an effective function of z , $g_{\text{eff}}(z, \bar{z})$, within the bin. Similarly, the unequal-time linear power spectrum of two narrow bins (with means

\bar{z}_1, \bar{z}_2) is given by

$$\begin{aligned} P_{\text{lin}}(k, z_1, z_2) &= P_{\text{lin}}(k)G(k, z_1)G(k, z_2) = P_{\text{lin}}(k)G(k, \bar{z}_1)G(k, \bar{z}_2)\frac{G(k, z_1)G(k, z_2)}{G(k, \bar{z}_1)G(k, \bar{z}_2)} \\ &\simeq \sqrt{P_{\text{lin}}(k, \bar{z}_1)P_{\text{lin}}(k, \bar{z}_2)}g_{\text{eff}}(z_1, \bar{z}_1)g_{\text{eff}}(z_2, \bar{z}_2) . \end{aligned} \quad (2.14)$$

Thus, for given narrow selection functions, the (k, z_1, z_2) -dependence can be approximated as separable and the integral can be solved in the same manner as before.

In general, one can always split the selection functions into narrow enough bins to make the approximation sufficiently accurate.

3 FFTLog and Beyond

The FFTLog algorithm was originally proposed in Ref. [28] to efficiently perform Hankel transforms (i.e., single-Bessel integrals), and was first applied to cosmology in Ref. [29]. In this section, we will first review the procedure of using FFTLog to compute an integral containing one spherical Bessel function (§3.1). Then, we generalize the algorithm to integrals with a Bessel function derivative (§3.2), which has applications including RSD.

3.1 Review of FFTLog

The FFTLog can be considered as the FFT of a logarithmically sampled integrand. Suppose we want to evaluate the integral

$$F(r) = \int_0^\infty \frac{dk}{k} f(k)j_\ell(kr) , \quad (3.1)$$

where $f(k)$ is a smooth input function sampled logarithmically in k . The FFTLog method first decomposes $f(k)$ into a series of power-laws, i.e.

$$f(k_q) = \frac{1}{N} \sum_{m=-N/2}^{N/2} c_m k_0^\nu \left(\frac{k_q}{k_0}\right)^{\nu+i\eta_m} , \quad (3.2)$$

where N is the sample size of the input function, $\eta_m = 2\pi m/(N\Delta_{\ln k})$, ν is the bias index, and $\Delta_{\ln k}$ is the linear spacing in $\ln(k)$, i.e., $k_q = k_0 \exp(q\Delta_{\ln k})$ with k_0 being the smallest value in the k array. The Fourier coefficients satisfy $c_m^* = c_{-m}$ since function $f(k)$ is real, and are computed by discrete Fourier transforming the “biased” input function $f(k)/k^\nu$ as

$$c_m = W_m \sum_{q=0}^{N-1} \frac{f(k_q)}{k_q^\nu} e^{-2\pi i m q/N} , \quad (3.3)$$

where W_m is a window function which smooths the edges of the c_m array and takes the form of Eq. (C.1) in [14]. This filtering is found to reduce ringing effects.

Each term is now analytically solvable with Eq. (A.3), i.e.

$$\begin{aligned} F(r) &= \frac{1}{Nr^\nu} \sum_{m=-N/2}^{N/2} c_m k_0^{-i\eta_m} r^{-i\eta_m} \int_0^\infty \frac{dx}{x} x^{\nu+i\eta_m} j_\ell(x) \\ &= \frac{\sqrt{\pi}}{4Nr^\nu} \sum_{m=-N/2}^{N/2} c_m k_0^{-i\eta_m} r^{-i\eta_m} g_\ell(\nu + i\eta_m) , \end{aligned} \quad (3.4)$$

where the first equality uses change of variable $x = kr$. The function $g_\ell(z)$ is given by

$$g_\ell(z) = 2^z \frac{\Gamma\left(\frac{\ell+z}{2}\right)}{\Gamma\left(\frac{3+\ell-z}{2}\right)}, \quad -\ell < \Re(z) < 2, \quad (3.5)$$

giving the allowed range of bias index $-\ell < \nu < 2$.

Finally, assuming that r is logarithmically sampled with the same linear spacing $\Delta_{\ln r} = \Delta_{\ln k}$ in $\ln r$, we can write the last summation in Eq. (3.4) as

$$F(r_p) = \frac{\sqrt{\pi}}{4r_p^\nu} \text{IFFT} [c_m^* (k_0 r_0)^{i\eta_m} g_\ell(\nu - i\eta_m)] , \quad (3.6)$$

where r_p ($p = 0, 1, \dots, N-1$) is the p -th element in the r array. IFFT stands for the Inverse Fast Fourier Transform. In summary, this method performs two FFT operations, one in computing c_m , one in the final summation over m . Thus, the total time complexity is $\mathcal{O}(N \log N)$.

3.2 Beyond FFTLog

One way to solve integrals involving a derivative of the Bessel function, such as

$$F_n(r) = \int_0^\infty \frac{dk}{k} f(k) j_\ell^{(n)}(kr) , \quad (3.7)$$

where superscript (n) stands for the n -th derivative, is to rewrite the derivative in terms of several Bessel functions of different orders using recurrence relations. However, it will inevitably increase the number of Hankel transforms if we were to use the original FFTLog method. In this subsection, we generalize the FFTLog method to directly compute this type of integral.

Following the same procedure of power-law decomposition, we can write Eq. (3.7) as

$$F_n(r) = \frac{1}{Nr^\nu} \sum_{m=-N/2}^{N/2} c_m k_0^{-i\eta_m} r^{-i\eta_m} \int_0^\infty \frac{dk}{k} k^{\nu+i\eta_m} j_\ell^{(n)}(k) . \quad (3.8)$$

Again, the integral for each m has an analytic solution, which can be shown with integration by parts. We write the solution in the same form as with the FFTLog, i.e.,

$$F_n(r) = \frac{\sqrt{\pi}}{4Nr^\nu} \sum_{m=-N/2}^{N/2} c_m k_0^{-i\eta_m} r^{-i\eta_m} \tilde{g}_\ell(n, \nu + i\eta_m) , \quad (3.9)$$

and its discrete version assuming $\Delta_{\ln r} = \Delta_{\ln k}$,

$$F_n(r_p) = \frac{\sqrt{\pi}}{4r_p^\nu} \text{FFT} [c_m^* (k_0 r_0)^{i\eta_m} \tilde{g}_\ell(n, \nu - i\eta_m)] , \quad (3.10)$$

where $\tilde{g}_\ell(n, z) = 4\pi^{-1/2} \int_0^\infty dk k^{z-1} j_\ell^{(n)}(k)$. For $n = 0$, $\tilde{g}_\ell(0, z) = g_\ell(z)$, and for $n = 1, 2$, it is given by (see Appendix A)

$$\tilde{g}_\ell(1, z) = -2^{z-1} (z-1) \frac{\Gamma\left(\frac{\ell+z-1}{2}\right)}{\Gamma\left(\frac{4+\ell-z}{2}\right)}, \quad \left(\begin{array}{l} 0 < \Re(z) < 2, \quad \text{for } \ell = 0 \\ 1 - \ell < \Re(z) < 2, \quad \text{for } \ell \geq 1 \end{array} \right), \quad (3.11)$$

$$\tilde{g}_\ell(2, z) = 2^{z-2} (z-1)(z-2) \frac{\Gamma\left(\frac{\ell+z-2}{2}\right)}{\Gamma\left(\frac{5+\ell-z}{2}\right)}, \quad \left(\begin{array}{l} -\ell < \Re(z) < 2, \quad \text{for } \ell = 0, 1 \\ 2 - \ell < \Re(z) < 2, \quad \text{for } \ell \geq 2 \end{array} \right). \quad (3.12)$$

We use $\nu = 1$ for all ℓ 's. With this generalized FFTLog algorithm, the integral containing one derivative of a spherical Bessel function also takes 2 FFT operations to compute.

4 Applications

Equipped with the generalized FFTLog algorithm, we are ready to compute the non-Limber angular power spectra of various tracers. In this section, we first demonstrate this for the galaxy clustering (§4.1). Then, we apply our algorithm to GGL (§4.2). For each application, we first convert the integrals to a form that is solvable with FFTLog or its extension, then we implement it to compute data vectors based on the LSST Y1 modeling, and compare the results to the results from a “brute-force” routine in `CosmoLike`[30].

4.1 Galaxy Clustering Power Spectrum

Background and Formalism In §2.1 and 2.2, we have shown that the “DD” component can be written as a nonlinear contribution, solved with the Limber approximation, and a linear part, solvable with the FFTLog. We now consider the full integral of C_ℓ^{gg} .

With the transfer function relations Eq. (2.5), the galaxy number count transfer function can be rewritten as

$$\begin{aligned} \Delta_\ell^{\text{g}} &= \int d\chi \left[\underbrace{n_z b \frac{H}{c} j_\ell(k\chi)}_{\text{Density}} - \underbrace{n_z f \frac{H}{c} j_\ell''(k\chi)}_{\text{RSD}} + \underbrace{\frac{3\ell(\ell+1)H_0^2\Omega_m(1+z(\chi))}{c^2k^2} W^{\text{M}} j_\ell(k\chi)}_{\text{Magnification}} \right] T_\delta(k, z(\chi)) \\ &= \int d\chi S^{\text{g}}(k, \chi) T_\delta(k, z(\chi)) , \end{aligned} \quad (4.1)$$

where $S^{\text{g}}(k, \chi)$ is defined as the terms in the square bracket for simplicity, and to make the equation more compact, we do not write out explicitly the z dependences of $n_z(z)$, $b(z)$, $H(z)$, $W^{\text{M}}(z)$. Substituting it into Eq. (2.7), we obtain

$$\begin{aligned} C_\ell^{\text{gg}} &= \frac{2}{\pi} \int_0^\infty \frac{dk}{k} k^3 \int d\chi_1 S^{\text{g}}(k, \chi_1) \int d\chi_2 S^{\text{g}}(k, \chi_2) P_\delta(k, z(\chi_1), z(\chi_2)) \\ &= \frac{2}{2\ell+1} \int_0^\infty dk (\tilde{\Delta}^{\text{g}}(\chi_\ell))^2 (P_\delta(k, z(\chi_\ell)) - P_{\text{lin}}(k, z_\ell)) \\ &\quad + \frac{2}{\pi} \int_0^\infty \frac{dk}{k} k^3 P_{\text{lin}}(k, 0) \left[\int \frac{d\chi_1}{\chi_1} \chi_1 S^{\text{g}}(k, \chi_1) G(z(\chi_1)) \right] \left[\int \frac{d\chi_2}{\chi_2} \chi_2 S^{\text{g}}(k, \chi_2) G(z(\chi_2)) \right] . \end{aligned} \quad (4.2)$$

The second term of the second equality is the linear matter power spectrum term with separable redshift evolution. The integral in each square bracket can be further broken into three or two integrals (collecting terms with the same order of j_ℓ 's) solvable with FFTLog or its extension in §3. The first term of the second equality is the Limber approximation of the nonlinear contribution, where we reduce $S^{\text{g}}(k, \chi)$ to $\sqrt{\pi/(2\ell+1)} \tilde{\Delta}^{\text{g}}(\chi) \delta(\ell+1/2-k\chi)$ and then integrate over the χ_1, χ_2 integrals. For simplicity we define the modified transfer function (with the same dimension as k) $\hat{\Delta}^{\text{g}} = \hat{\Delta}^{\text{D}} + \hat{\Delta}^{\text{RSD}} + \hat{\Delta}^{\text{M}}$, whose components are

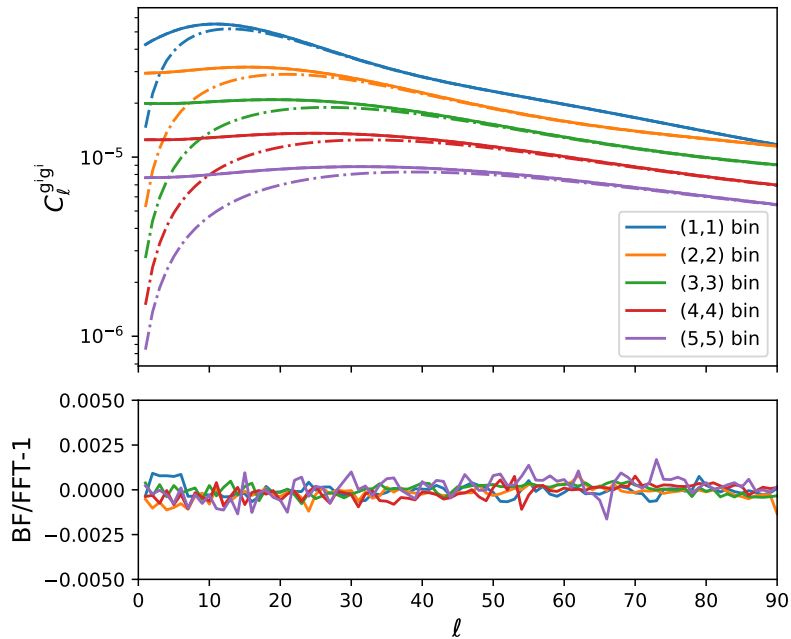


Figure 2. (*Upper panel:*) the non-Limber galaxy clustering auto power spectra C_ℓ^{gal} 's of the 5 lens tomographic bins in LSST Y1 from the FFT method (solid lines) and the brute-force integration (dashed lines) up to $\ell = 90$, along with the Limber results (dash-dotted lines). The FFT and the BF lines nearly overlap with each other. (*Lower panel:*) fractional differences between the BF and the FFT non-Limber results. The fractional differences are all within 0.2%, consistent with the numerical accuracy of our BF integration.

given by (also see Eqs. (75-77) in [7])

$$\tilde{\Delta}^{\text{D}}(\chi_\ell) = \frac{1}{c} n_z(z(\chi_\ell)) b(z(\chi_\ell)) H(z(\chi_\ell)) , \quad (4.3)$$

$$\tilde{\Delta}^{\text{RSD}}(\chi_\ell) = \frac{1 + 8\ell}{(2\ell + 1)^2} \frac{f(z(\chi_\ell))}{b(z(\chi_\ell))} \tilde{\Delta}^{\text{D}}(\chi_\ell) - \frac{4}{2\ell + 3} \sqrt{\frac{2\ell + 1}{2\ell + 3}} \frac{f(z(\chi_{\ell+1}))}{b(z(\chi_{\ell+1}))} \tilde{\Delta}^{\text{D}}(\chi_{\ell+1}) , \quad (4.4)$$

$$\tilde{\Delta}^{\text{M}}(\chi_\ell) = \frac{3\ell(\ell + 1)\Omega_{\text{m}}H_0^2(1 + z(\chi_\ell))}{c^2k^2} W^{\text{M}}(\chi_\ell) , \quad (4.5)$$

where the RSD term is derived using the recurrence relations of spherical Bessel functions and approximating the Bessel functions as delta functions.

Results We compute the galaxy clustering power spectra for LSST Y1, as described in §5, using our FFTLog method and using a brute-force (BF) quadrature integration. In the upper panel of Figure 2 we show in solid lines the non-Limber galaxy clustering power spectra C_ℓ^{gal} calculated with our FFT method, and in dashed lines the BF quadrature integration. We also plot the Limber result in dash-dotted lines. In the lower panel, we show the fractional differences between the BF and the FFT non-Limber results (BF/FFT-1). To speed up the BF calculations, we require a 1% accuracy of the quadrature integration of the non-Limber part and 0.1% accuracy of the Limber integrals. The fractional differences are all within 0.2%.

4.2 Galaxy-Galaxy Lensing Power Spectrum

Background and Formalism Galaxy-galaxy lensing (GGL) is the correlation between the shape of background (or *source*) galaxies and foreground (*lens*) galaxy number density. In the weak lensing regime, the observed galaxy shape, e is the sum of an intrinsic (unlensed) component and a shear, γ , due to gravitational lensing. We write their transfer function for the source galaxy shape as $\Delta^e = \Delta^\gamma + \Delta^{\text{IA}}$.

Again with the notations in Ref. [7], the lensing effect is characterized by

$$\Delta_\ell^\gamma = -\frac{1}{2}\sqrt{\frac{(\ell+2)!}{(\ell-2)!}} \int \frac{dz}{cH(z)} W^{\text{L}}(z) T_{\phi+\psi}(k, z) j_\ell(k\chi(z)), \quad (4.6)$$

where we have put back the constant c to make Δ_ℓ^{L} dimensionless. The lensing kernel W^{L} is given by

$$W^{\text{L}}(z) = \int_z^\infty dz' n_{\text{src}}(z') \frac{\chi(z') - \chi(z)}{\chi(z')\chi(z)}, \quad (4.7)$$

where $n_{\text{src}}(z)$ is the redshift distribution of the source galaxies. We use the ‘‘nonlinear linear alignment model’’ of IA (e.g., [31–37], but see [16] for limitations), which gives

$$\Delta_\ell^{\text{IA}} = \sqrt{\frac{(\ell+2)!}{(\ell-2)!}} \int dz n_{\text{src}}(z) A_{\text{IA}}(z) T_\delta(k, z) \frac{j_\ell(k\chi(z))}{|k\chi(z)|^2}, \quad (4.8)$$

where $A_{\text{IA}}(z)$ is the (dimensionless) alignment amplitude, defined by¹²

$$A_{\text{IA}} = -\frac{C_{1\rho_{\text{cr}}}\Omega_{\text{m}}}{G(z)} A_0 \left(\frac{\bar{L}}{L_0}\right)^\beta \left(\frac{1+z}{1+z_0}\right)^\eta = -\frac{C_{1\rho_{\text{cr}}}\Omega_{\text{m}}}{G(z)} a_{\text{IA}} \left(\frac{1+z}{1+z_0}\right)^\eta, \quad (4.9)$$

where we use $C_{1\rho_{\text{cr}}} \simeq 0.0134$, a normalization derived from SuperCOSMOS observations[32, 39], z_0, L_0 are arbitrary pivot values for the power-law scalings of the redshift (with index parameter η) and luminosity (with index parameter β) dependences, and \bar{L} is the weighted average luminosity of the source sample. We reduce the number of free parameters by combining free normalization factor A_0 and the luminosity dependence into a single free parameter a_{IA} . We take $z_0 = 0.62$ in our analysis, following the DES Year 1 choice in [40]. Combining the two pieces, we obtain the shear transfer function

$$\begin{aligned} \Delta_\ell^e &= \int d\chi \left\{ \sqrt{\frac{(\ell+2)!}{(\ell-2)!}} \left[\underbrace{\frac{3H_0^2\Omega_{\text{m}}(1+z(\chi))}{2c^2k^2}}_{\text{Lensing}} W^{\text{L}} + \underbrace{\frac{n_{\text{src}}A_{\text{IA}}H}{ck^2\chi^2}}_{\text{IA}} \right] j_\ell(k\chi) \right\} T_\delta(k, z(\chi)) \\ &= \int d\chi S^e(k, \chi) T_\delta(k, z(\chi)), \end{aligned} \quad (4.10)$$

where S^e is defined as the terms in the curly bracket, and we have again dropped the z dependences of $n_{\text{src}}(z), A_{\text{IA}}(z), H(z), W^{\text{L}}(z)$ for compactness.

¹²Our definition of A_{IA} absorbs the typical normalization factors for IA amplitude and redshift evolution, as well as the fraction of aligned galaxies in the sample. It is equivalent to $F(z)$ defined in Eq. (8) of Ref. [38].

Thus, the GGL angular power spectrum C_ℓ^{ge} is

$$\begin{aligned}
C_\ell^{\text{ge}} &= \frac{2}{\pi} \int_0^\infty \frac{dk}{k} k^3 \int d\chi_1 S^{\text{g}}(k, \chi_1) \int d\chi_2 S^{\text{e}}(k, \chi_2) P_\delta(k, z(\chi_1), z(\chi_2)) \\
&= \frac{2}{2\ell+1} \int_0^\infty dk \tilde{\Delta}^{\text{g}}(\chi_\ell) \tilde{\Delta}^{\text{e}}(\chi_\ell) (P_\delta(k, z(\chi_\ell)) - P_{\text{lin}}(k, z_\ell)) \\
&\quad + \frac{2}{\pi} \int_0^\infty \frac{dk}{k} k^3 P_{\text{lin}}(k, 0) \left[\int \frac{d\chi_1}{\chi_1} \chi_1 S^{\text{g}}(k, \chi_1) G(z(\chi_1)) \right] \left[\int \frac{d\chi_2}{\chi_2} \chi_2 S^{\text{e}}(k, \chi_2) G(z(\chi_2)) \right], \tag{4.11}
\end{aligned}$$

where we reduce $S^e(k, \chi)$ to $\sqrt{\pi/(2\ell+1)} \tilde{\Delta}^e(\chi) \delta(\ell+1/2 - k\chi)$ and integrate over χ_1, χ_2 in the Limber approximation. We also define the modified transfer function (with the same dimension as k) $\tilde{\Delta}^e = \tilde{\Delta}^\gamma + \tilde{\Delta}^{\text{IA}}$ for simplicity, whose components are given by (also see Eqs. (78-79) in [7])

$$\tilde{\Delta}^\gamma(\chi_\ell) = \sqrt{\frac{(\ell+2)!}{(\ell-2)!} \frac{3\Omega_{\text{m}} H_0^2 (1+z(\chi_\ell))}{2c^2 k^2}} W^{\text{L}}(z(\chi_\ell)), \tag{4.12}$$

$$\tilde{\Delta}^{\text{IA}}(\chi_\ell) = \sqrt{\frac{(\ell+2)!}{(\ell-2)!} \frac{n_{\text{src}}(z(\chi_\ell)) A_{\text{IA}}(z(\chi_\ell)) H(z(\chi_\ell))}{c(\ell+1/2)^2}}. \tag{4.13}$$

Similar to the case of galaxy clustering, the integrals in the linear part can be evaluated with FFTLog and its extension discussed in §3.

Results We compute the GGL power spectra for LSST Y1, as described in §5, using our FFTLog method and using a brute-force (BF) quadrature integration. In Figure 3, on the upper panel we show in solid lines the non-Limber angular power spectra of the 4th lens tomographic bin and all the 5 source bins calculated with our FFT method, in dashed lines with the BF quadrature integration. We also plot the Limber results in dash-dotted lines. On the lower panel, we show the fractional differences between the BF and the FFT non-Limber results (BF/FFT-1). To speed up the BF calculations, we require a 1% accuracy of the quadrature integration of the non-Limber part and 0.1% accuracy of the Limber integrals. The fractional differences are mostly within 1%. Larger errors occur near the zero-crossing in the power spectra. Large differences between the Limber and non-Limber occur in, for example, the cross power spectrum between the 4th lens bin and the 3rd source bin, where two bins largely overlap and the overlapping part of the selection functions are narrow. We test all other 20 lens-source bin combinations of GGL power spectra in Appendix B.

5 Significance for Future Survey Analyses

The capability of efficient modeling of angular power spectra beyond the Limber approximation enables us to assess the impact of the Limber approximation on the parameter constraints in future cosmological analyses. We present simulated likelihood analyses of galaxy clustering, GGL and cosmic shear for LSST Y1 and DES Y6.

5.1 Analysis Ingredients

5.1.1 Lens and Source Galaxy Sample Distributions

We generate the redshift distributions of the lens and source galaxies in LSST Y1 following the DESC Science Requirements Document (DESC SRD, [1]). The LSST Y1 survey will

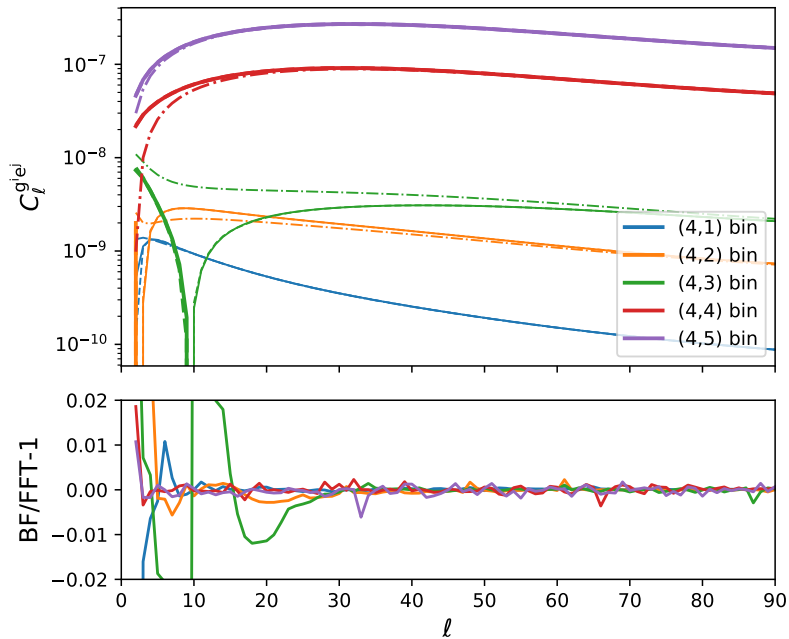


Figure 3. (*Upper panel:*) the non-Limber GGL power spectra C_ℓ^{ggl} of the 4th lens tomographic bin and all the 5 source bins in LSST Y1 from the FFT method (solid lines) and the brute-force integration (dashed lines) up to $\ell = 90$, along with the Limber results (dash-dotted lines). The FFT and the BF lines nearly overlap with each other. (*Lower panel:*) fractional differences between the BF and the FFT non-Limber results. The fractional differences are mostly within 1%, consistent with the numerical accuracy of our BF integration. Larger errors occur near the zero-crossing in the power spectra.

have a survey area of 12.3k deg^2 and is expected to measure galaxies with an i-band depth $i_{\text{depth}} = 25.1$ mag for the weak lensing (source sample) and galaxies with an i-band limit $i_{\text{lim}} = i_{\text{depth}} - 1 = 24.1$ mag for the large-scale structure (lens sample). For the lens sample, we use a parametric redshift distribution (same as Eq. (5) in Appendix D1.1 of the DESC SRD)

$$\frac{dN}{dz} \propto z^2 \exp[-(z/z_0)^\alpha], \quad (5.1)$$

with $(z_0, \alpha) = (0.26, 0.94)$, normalized by the effective number density $n_{\text{eff}} = 18 \text{ arcmin}^{-2}$. We divide the sample into 5 tomographic bins with equal number of galaxies and convolve each bin with a Gaussian photo- z scatter with $\sigma_z = 0.03(1+z)$. For each tomographic bin i , we set their fiducial linear galaxy bias parameters as $b_i = 1.05/G(\bar{z}^i)$, where \bar{z}^i is the mean redshift of the i -th bin, and $G(z)$ is the linear growth factor. For the source sample, we use the same parametric form but with $(z_0, \alpha) = (0.191, 0.870)$, normalized to $n_{\text{eff}} = 11.2 \text{ arcmin}^{-2}$.¹³ We also divide the source sample into 5 equally populated tomographic bins and convolve each bin with a Gaussian photo- z uncertainty with $\sigma_z = 0.05(1+z)$. The distributions of the lens and source tomographic bins are shown on the left panel of Figure 4. We assume the galaxy shape noise to be $\sigma_e = 0.26$ per component.

¹³These values for the source sample are the updated version from private communication with Rachel Mandelbaum.

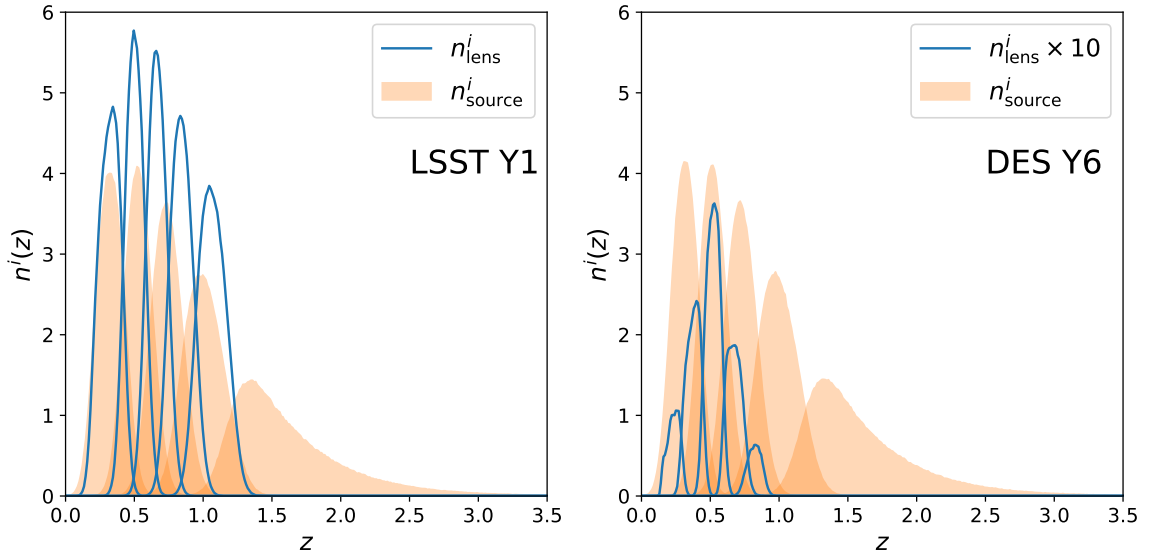


Figure 4. The redshift distributions of the lens and source samples for LSST Y1 (*left*) and DES Y6 (*right*). Each sample is split into 5 bins, as described in §5.1.1.

The full DES survey (Y6) has a survey area of 5000 deg^2 and is expected to measure galaxies with very similar depth to the LSST Y1. Therefore, we define the source sample to reach i -depth of 25.0 mag and follow the same parametric redshift distribution. Using fitting formulae from the DESC SRD, we obtain $(z_0, \alpha) = (0.193, 0.876)$ and $n_{\text{eff}} = 10.47 \text{ arcmin}^{-2}$. Similar to LSST Y1, we divide the source sample into 5 equally populated tomographic bins with $\sigma_z = 0.05(1+z)$, but set the shape noise consistent with DES Y1, i.e., $\sigma_e = 0.279$ per component. For the lens sample, we assume a REDMAGIC [41] selected sample and split it into 5 bins similar to the DES Y1 analysis [42, 43]. We show the distributions of the lens and source tomographic bins on the right panel of Figure 4.

5.1.2 Angular Two-Point Functions

The modeling of the galaxy clustering power spectra and the GGL power spectra has already been shown in §4.1 and 4.2. We model cosmic shear using the Limber approximation as the lensing efficiency function is very broad. Including IA and following the notation in §4.2, the tomographic cosmic shear power spectra between the source bin i and j can be written as

$$C_\ell^{e^i e^j} = \frac{2}{2\ell + 1} \int_0^\infty dk \tilde{\Delta}^{e^i}(\chi_\ell) \tilde{\Delta}^{e^j}(\chi_\ell) P_\delta(k, z(\chi_\ell)). \quad (5.2)$$

We compute the linear matter power spectrum using CLASS [44], and the nonlinear matter power spectrum with HALOFIT [45]. To perform likelihood analyses real space, we calculate the angular two-point correlation functions for galaxy clustering $w^i(\theta)$, GGL $\gamma_t^{ij}(\theta)$, and cosmic

shear $\xi_{+/-}^{ij}(\theta)$, using their relation to angular power spectra on the curved sky:

$$w^i(\theta) = \sum_{\ell} \frac{2\ell+1}{4\pi} P_{\ell}(\cos\theta) C^{\mathbf{g}^i \mathbf{g}^i}(\ell), \quad (5.3)$$

$$\gamma_t^{ij}(\theta) = \sum_{\ell} \frac{2\ell+1}{4\pi\ell(\ell+1)} P_{\ell}^2(\cos\theta) C^{\mathbf{g}^i \mathbf{e}^j}(\ell), \quad (5.4)$$

$$\xi_{\pm}^{ij}(\theta) = \sum_{\ell} \frac{2\ell+1}{2\pi\ell^2(\ell+1)^2} [G_{\ell,2}^+(\cos\theta) \pm G_{\ell,2}^-(\cos\theta)] C^{\mathbf{e}^i \mathbf{e}^j}(\ell), \quad (5.5)$$

where θ is the angular separation, P_{ℓ} and P_{ℓ}^2 are the Legendre polynomial and the associated Legendre polynomial, $G_{\ell,m}^{+/-}$ are given by Eq. (4.19) of [46]. We have used the indices i, j to denote the tomographic bins involved, i.e., $C^{\mathbf{g}^i \mathbf{g}^i}(\ell)$ is the galaxy clustering power spectrum of the i -th lens tomographic bin, $C^{\mathbf{g}^i \mathbf{e}^j}(\ell)$ is the GGL power spectrum of the i -th lens tomographic bin and the j -th source bin, and $C^{\mathbf{e}^i \mathbf{e}^j}(\ell)$ is the tomographic cosmic shear power spectrum of the i -th and j -th source bins.

We compute all correlation functions in 26 logarithmically spaced angular bins over the range $2.5' < \theta < 900'$. For each angular bin $[\theta_{\min}, \theta_{\max}]$, the correlation functions are bin-averaged, i.e., replacing $P_{\ell}(\cos\theta)$, $P_{\ell}^2(\cos\theta)$ and $[G_{\ell,2}^+(\cos\theta) \pm G_{\ell,2}^-(\cos\theta)]$ with their bin-averaged functions $\overline{P_{\ell}}$, $\overline{P_{\ell}^2}$ and $\overline{G_{\ell,2}^+ \pm G_{\ell,2}^-}$ [47], defined by

$$\overline{P_{\ell}} = \frac{\int_{\cos\theta_{\min}}^{\cos\theta_{\max}} dx P_{\ell}(x)}{\cos\theta_{\max} - \cos\theta_{\min}} = \frac{[P_{\ell+1}(x) - P_{\ell-1}(x)]_{\cos\theta_{\min}}^{\cos\theta_{\max}}}{(2\ell+1)(\cos\theta_{\max} - \cos\theta_{\min})}, \quad (5.6)$$

$$\overline{P_{\ell}^2} = \frac{\int_{\cos\theta_{\min}}^{\cos\theta_{\max}} dx P_{\ell}^2(x)}{\cos\theta_{\max} - \cos\theta_{\min}} = \frac{[(\ell + \frac{2}{2\ell+1})P_{\ell-1}(x) + (2-\ell)xP_{\ell}(x) - \frac{2}{2\ell+1}P_{\ell+1}(x)]_{\cos\theta_{\min}}^{\cos\theta_{\max}}}{\cos\theta_{\max} - \cos\theta_{\min}} \quad (5.7)$$

$$\begin{aligned} \overline{G_{\ell,2}^+ \pm G_{\ell,2}^-} &= \frac{1}{\cos\theta_{\max} - \cos\theta_{\min}} \left\{ -\frac{\ell(\ell-1)}{2}(\ell + \frac{2}{2\ell+1})P_{\ell-1}(x) - \frac{\ell(\ell-1)(2-\ell)}{2}xP_{\ell}(x) + \frac{\ell(\ell-1)}{2\ell+1}P_{\ell+1}(x) \right. \\ &\quad \left. + (4-\ell)\frac{dP_{\ell}(x)}{dx} + (\ell+2)[x\frac{dP_{\ell-1}(x)}{dx} - P_{\ell-1}(x)] \pm 2(\ell-1)[x\frac{dP_{\ell}(x)}{dx} - P_{\ell}(x)] \mp 2(\ell+2)\frac{dP_{\ell-1}(x)}{dx} \right\}_{\cos\theta_{\min}}^{\cos\theta_{\max}}. \end{aligned} \quad (5.8)$$

Our analysis includes all auto-correlations of the lens bins for the galaxy clustering, all combinations of lens and source bins for the GGL, and all auto- and cross-correlations of the source bins for the cosmic shear. Thus, for each survey, the data vector contains 5 sets of $w(\theta)$, 25 sets of $\gamma_t(\theta)$, 15 sets of $\xi_+(\theta)$ and 15 sets of $\xi_-(\theta)$, each of which has 26 angular bins.

5.1.3 Systematics

Systematic uncertainties are parameterized through nuisance parameters in a similar way to the DES Y1 analysis [48].

Photometric redshift uncertainties The uncertainty in the redshift distribution of the i -th tomographic bin $n^i(z)$ is modeled by one shift parameter Δ_z for each bin of the lens and the source samples, i.e., $n^i(z) = \hat{n}^i(z - \Delta_z^i)$, where the index i traverses over all the lens and source bins, and \hat{n} is the estimated redshift distribution as described in §5.1.1. There are 10 shift parameters in total. We take 0 as their fiducial values to generate the simulated data vector, and marginalize over them in the likelihood analyses. For the lens sample in both surveys, we choose a Gaussian prior with $\mu = 0, \sigma = 0.005(1 + \bar{z}^i)$ for each $\Delta_{z,\text{lens}}^i$. For the

source samples in both surveys, we choose a Gaussian prior with $\mu = 0, \sigma = 0.002(1 + \bar{z}^i)$ for each $\Delta_{z,\text{source}}^i$, consistent with the requirements given in §5.1 and 5.2 of the DESC SRD.

Galaxy bias We assume a linear bias model and use one parameter for each lens bin. There are 5 parameters in total, whose fiducial values are described in §5.1.1 for generating the simulated data vector. In the likelihood analysis, they will be marginalized over with conservative flat priors (between 0.8 and 3).

Lensing magnification bias Lensing magnification was not included in the baseline model of DES Y1 analysis. We parameterize the effect through one parameter for each lens bin b_{mag}^i . For magnitude limited samples, magnification due to lensing by line-of-sight structure can affect the number density of galaxies with observed magnitudes exceeding the magnitude cut (e.g., [21–23]). For LSST Y1, we assume the lens samples are magnitude limited. Using the fitting formulae in Appendix C¹⁴ of [51] and an r -band limit of 24.81 mag (see Appendix C1 of the DESC SRD and define r -band limit for lens sample $r_{\text{lim}} = r_{\text{depth}} - 1 = 25.81 - 1$ mag), we obtain $b_{\text{mag}}^i = (-0.898, -0.659, -0.403, -0.0704, 0.416)$ for the 5 lens bins. For DES Y6 lens sample, we use luminosity cuts $L/L_* > (0.5, 0.5, 0.5, 1.0, 1.0)$ for bins from low to high redshifts, respectively. L_* is the characteristic galaxy luminosity where the power-law form in the Schechter luminosity function cuts off [52]. To estimate b_{mag} , we assume a Schechter luminosity function $N(L) \propto (L/L_*)^\alpha \exp(-L/L_*)$, where the parameter α characterizes the faint-end slope, $N(L)$ is the number of galaxies per unit luminosity bin. b_{mag} is related to the luminosity function by

$$b_{\text{mag}} = -2 - 2 \left. \frac{d \log_{10} N_{>L}}{d \log_{10} L} \right|_{L=L_{\text{lim}}} = -2 + 2 L_{\text{lim}} \frac{N(L_{\text{lim}})}{N_{>L_{\text{lim}}}} = -2 + 2 \frac{\left(\frac{L_{\text{lim}}}{L_*}\right)^{\alpha+1} e^{-L_{\text{lim}}/L_*}}{\Gamma(\alpha+1, L_{\text{lim}}/L_*)}, \quad (5.9)$$

where L_{lim} is the luminosity cut, and $N_{>L}$ is the number of galaxies brighter than luminosity L , calculated by integrating the luminosity function. $\Gamma(a, z)$ is the incomplete Gamma function¹⁵. We assume a constant $\alpha = -0.8$ for all lens bins, leading to $b_{\text{mag}}^i = (-0.102, -0.102, -0.102, 1.06, 1.06)$. Note that these values may not represent the exact values for the REDMAGIC sample, but merely our approximate choice for generating the fiducial simulated data vector. Although we haven't considered other selection biases, such as the size magnification bias due to the magnification of the angular sizes of source galaxies, the uncertainties of their effects are encapsulated in the 5 nuisance parameters b_{mag}^i and are marginalized over conservative flat priors (between -3 and 3) in the likelihood analysis.

Multiplicative shear calibration We use one shear calibration uncertainty parameter m^i per source bin (5 in total), acting on the cosmic shear and GGL correlation functions such that

$$\begin{aligned} \xi_{+/-}^{ij}(\theta) &\rightarrow (1 + m^i)(1 + m^j) \xi_{+/-}^{ij}(\theta), \\ \gamma_t^{ij}(\theta) &\rightarrow (1 + m^j) \gamma_t^{ij}(\theta). \end{aligned} \quad (5.10)$$

They are marginalized over independently with Gaussian priors ($\mu = 0, \sigma = 0.005$).

¹⁴based on the relation between the galaxy redshift distributions and the magnitude limits modeled by [49] using COMBO-17 luminosity functions for the SDSS r filter [50].

¹⁵The incomplete Gamma function is defined as $\Gamma(a, z) = \int_z^\infty t^{a-1} e^{-t} dt$. See e.g., Eq. (8.2.2) of DLMF [53].

IA We use the nonlinear linear alignment (NLA) model and parameterize it with two parameters a_{IA} and η . See §4.2 for detail. Their fiducial values are $a_{\text{IA}} = 0.5$ and $\eta = 0$, and they are both marginalized over independently with conservative flat priors between -5 and 5 .

5.1.4 Covariances

The Fourier space 3x2pt covariances, including the Gaussian part [54], the connected non-Gaussian part (calculate with the halo model) and the super-sample covariance [55], are described in Appendix A of [30]. We calculate the covariances of bin-averaged correlation functions on the curved sky, i.e., for two angular two-point functions, $\Xi, \Theta \in \{w, \gamma_t, \xi_+, \xi_-\}$

$$\text{Cov}(\Xi^{ij}(\theta), \Theta^{km}(\theta')) = \sum_{\ell} \overline{P_{\ell}^{\Xi}} \sum_{\ell'} \overline{P_{\ell'}^{\Theta}} \text{Cov}(C_{\Xi}^{ij}(\ell), C_{\Theta}^{km}(\ell')), \quad (5.11)$$

where $C_{\xi_+} = C_{\xi_-} = C^{ee}$, $C_{\gamma_t} = C^{\text{ge}}$, and $C_w = C^{\text{gg}}$ in our previous notation, and i, j, k, m are the tomographic bin indices. The bin-averaged weight functions are defined as [47]

$$\overline{P_{\ell}^w} = \frac{2\ell + 1}{4\pi} \overline{P_{\ell}} = \frac{[P_{\ell+1}(x) - P_{\ell-1}(x)]_{\cos \theta_{\min}}^{\cos \theta_{\max}}}{4\pi(\cos \theta_{\max} - \cos \theta_{\min})}, \quad (5.12)$$

$$\overline{P_{\ell}^{\gamma_t}} = \frac{2\ell + 1}{4\pi\ell(\ell + 1)} \overline{P_{\ell}^2} = \frac{2\ell + 1}{4\pi\ell(\ell + 1)} \frac{[(\ell + \frac{2}{2\ell+1})P_{\ell-1}(x) + (2 - \ell)xP_{\ell}(x) - \frac{2}{2\ell+1}P_{\ell+1}(x)]_{\cos \theta_{\min}}^{\cos \theta_{\max}}}{\cos \theta_{\max} - \cos \theta_{\min}}, \quad (5.13)$$

$$\overline{P_{\ell}^{\xi_{\pm}}} = \frac{2\ell + 1}{2\pi\ell^2(\ell + 1)^2} \overline{G_{\ell,2}^{\pm}}, \quad (5.14)$$

In practice, we evaluate Eq. (5.11) up to $\ell_{\max} = 50000$.

5.1.5 Angular Scale Cuts

Limited by our ability to accurately model the non-linearities of the density and galaxy fields on small scales, survey analyses define a set of angular scale cuts, preventing nonlinear modeling limitations from biasing the cosmology results. In accordance with the DESC SRD, we choose a Fourier scale cut $k_{\max} = 0.3h/\text{Mpc}$, which roughly corresponds to a comoving scale $R_{\min} = 2\pi/k_{\max} = 21 \text{ Mpc}/h$.

For the galaxy clustering, we define the angular scale cut θ_{\min}^i for lens tomographic bin i as

$$\theta_{\min}^i = \frac{R_{\min}}{\chi(\bar{z}^i)}, \quad (5.15)$$

where \bar{z}^i is the mean redshift of galaxies in redshift bin i . For our LSST Y1 lens sample, θ_{\min}^i are $80.88'$, $54.19'$, $42.85'$, $35.43'$, $29.73'$, respectively. For DES Y6, they are $108.3'$, $69.77'$, $52.53'$, $42.37'$, $36.15'$. For the GGL γ_t^{ij} , we use the same angular cuts as θ_{\min}^i .

For the cosmic shear, we use the Fourier scale cut defined in the DESC SRD, i.e., $\ell < \ell_{\max} = 3000$, and translate it into the angular cuts for $\xi_{+/-}$ with the first zeros of their corresponding Bessel functions $J_{0/4}$ (in the flat-sky-limit transform), i.e., $\theta_{\min}^{\xi_+} = 2.4048/\ell_{\max} = 2.756'$, and $\theta_{\min}^{\xi_-} = 7.5883/\ell_{\max} = 8.696'$.

5.2 Simulated Likelihood Analysis

The parameter estimation is done by sampling and maximizing the likelihood of the data \mathbf{D} given a point in cosmological and nuisance parameter space \mathbf{p} ,

$$L(\mathbf{D}|\mathbf{p}) \propto \exp\left(-\frac{1}{2} [(\mathbf{D} - \mathbf{M}(\mathbf{p}))^T \mathbf{C}^{-1} (\mathbf{D} - \mathbf{M}(\mathbf{p}))]\right), \quad (5.16)$$

where \mathbf{M} is the model vector and \mathbf{C} is the covariance matrix. We generate the simulated 3x2pt data vector \mathbf{D} by computing the model vector at the fiducial parameter values and in our fiducial cosmology (standard Λ CDM with massless neutrinos), with non-Limber modeling of w and γ_t , and Limber modeling of $\xi_{+/-}$, as described in §5.1.2. Throughout our analyses, we use the `emcee` sampler [56].

5.2.1 The Impact of Limber Approximation

To evaluate the impact of the Limber approximation in the configurations of LSST Y1 and DES Y6, we fit the data vector with a set of models:

- Model (I): A 2x2pt (galaxy clustering + GGL) analysis which uses the Limber approximation to calculate w, γ_t ;
- Model (II): A cosmic shear analysis which uses the Limber approximation to calculate $\xi_{+/-}$;
- Model (III): A 3x2pt analysis which uses the Limber approximation to calculate all 3x2pt correlations;
- Model (IV): A 2x2pt analysis which uses the Limber approximation to calculate γ_t and uses our non-Limber method to compute w .

We summarize the fiducial values and priors of the parameters in Table 1.

In Figure 5, we show the 1σ and 2σ contours of the 3 cosmological parameters (Ω_m, σ_8, n_s) as well as their marginalized 1D distributions from Models (I-III), in the cases of LSST Y1 and DES Y6, respectively. The Limber approximation modifies the angular power spectra at low- ℓ , which results in the bias of the spectral index n_s for Model (I), the Limber 2x2pt model. For both surveys, n_s absorbs most of the cosmological parameter biases. However, since cosmic shear has stronger constraining power on n_s , the combined 3x2pt result is shifted towards the fiducial n_s values, while other parameters may be shifted further away from the fiducial values. For the $\Omega_m - \sigma_8$ contour, we see a shift greater than 1σ for LSST Y1, and a nearly 1σ shift for DES Y6.

Taking LSST Y1 as an example, in Figure 6, we show the 1σ and 2σ contours of the 3 cosmological parameters (Ω_m, σ_8, n_s) as well as their marginalized 1D distributions from Models (I) and (IV). These contours show that using the non-Limber model of w only can effectively correct the biases induced by the Limber approximation, and a full non-Limber model of both w and γ_t is not necessary for the analyses considered in this paper. Model (IV) also takes significantly less computation time than a full non-Limber model of both w and γ_t , as there are 25 GGL angular correlations and only 5 galaxy clustering auto-correlations. We also note that the goodness of the fit is largely improved from Model I (best-fit $\chi^2 = 76.0$) to Model IV (best-fit $\chi^2 = 8.3$), where $\chi^2 = (\mathbf{D} - \mathbf{M})^T \mathbf{C}^{-1} (\mathbf{D} - \mathbf{M})$. In the parameter space, we can define the parameter distance $d_{\mathbf{p}}$ between the best-fit parameters \mathbf{p}_{fit} and the

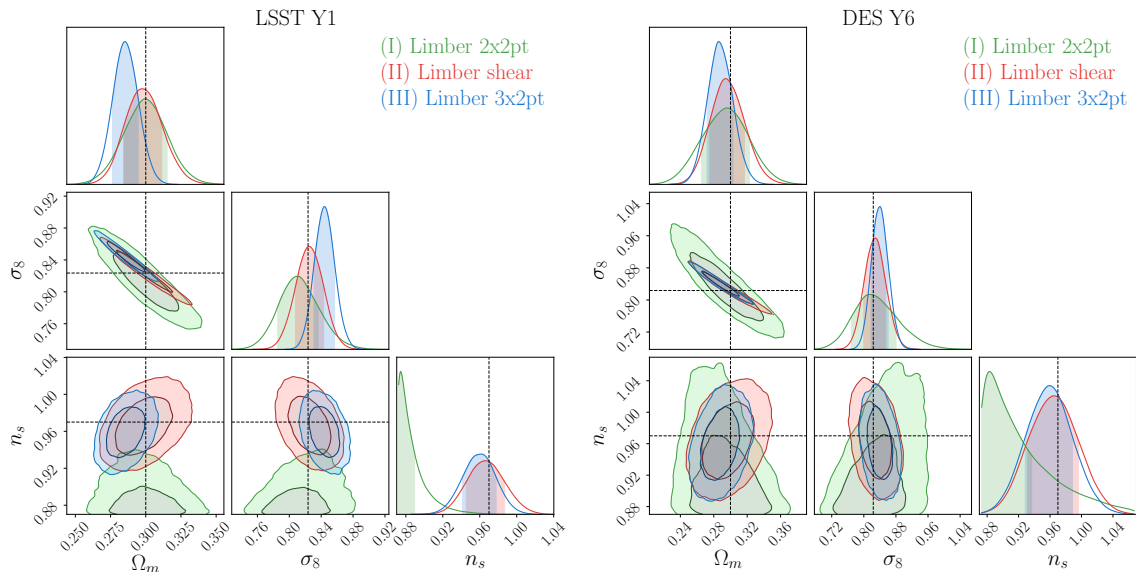


Figure 5. The 1σ and 2σ contours of fitting the simulated (non-Limber $w + \gamma_t$, Limber ξ_{\pm}) 3x2pt data vector \mathbf{D} with Models (I) Limber 2x2pt ($w + \gamma_t$, in green), (II) Limber shear (ξ_{\pm} , in red), (III) Limber 3x2pt (in blue), for LSST Y1 (*left*) and DES Y6 (*right*). The dashed lines mark the fiducial values. In both surveys, Model (I) introduces significant biases to n_s , while Ω_m, σ_8 are less affected. Model (II) correctly recovers fiducial values of all the parameters as expected. Model (III) gains an improved n_s constraint from the cosmic shear, forcing the other two parameters to shift away from their fiducial values by $\sim 1\sigma$.

fiducial parameters \mathbf{p}_0 as $d_{\mathbf{p}}^2 = (\mathbf{p}_{\text{fit}} - \mathbf{p}_0)^T \mathbf{C}_{\mathbf{p}}^{-1} (\mathbf{p}_{\text{fit}} - \mathbf{p}_0)$, where the parameter covariance $\mathbf{C}_{\mathbf{p}}$ is measured from the chain output. Taking the parameter space of $(\Omega_m, \sigma_8, n_s, \Omega_b, h_0)$, we find that $d_{\mathbf{p}}^2$ improves from 31.8 (Model I) to 2.7 (Model IV).

5.2.2 The Impact of n_s Priors

The impact of the Limber approximation is largely absorbed through a bias in n_s , on which the 2x2pt probes don't have a good constraining power. However, n_s is very well constrained by CMB experiments like Planck. By using a more informative prior of n_s , other cosmological parameters may be impacted more significantly by the Limber approximation, similar to the shift in parameters from including the cosmic shear in Model (III) as shown in Figure 5.

We demonstrate this by fitting the data vector \mathbf{D} with Model (I) but with a Gaussian prior of n_s , centered at our fiducial value 0.97 with width equal to the 1σ error bar of Planck 2018, i.e., $\sigma = 0.0038$, (TT,TE,EE+lowE+lensing+BAO) [57]. We show the comparison between the constraints from this Gaussian prior and from the flat prior [0.87,1.07] in Figure 7 for LSST Y1. We find that by imposing an informative prior on n_s , the posterior of n_s is pushed back to around the fiducial value, while the other cosmological parameters Ω_m, σ_8 are significantly shifted. With the 1xPlanck Gaussian prior of n_s , we find that the goodness of the fit is worse in the data vector space with the best-fit χ^2 going from 76.0 to 88.6, but is better in the cosmological parameter space $(\Omega_m, \sigma_8, n_s, \Omega_b, h_0)$ with $d_{\mathbf{p}}^2$ dropping from 31.8 to 15.9.

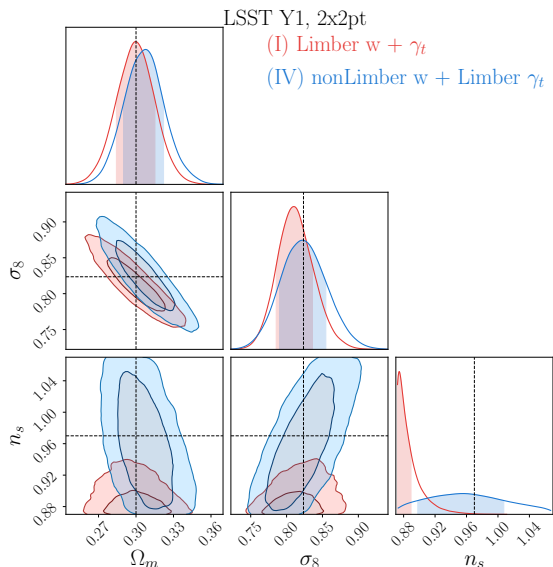


Figure 6. The 1σ and 2σ contours of fitting the LSST Y1 simulated (non-Limber $w + \gamma_t$) 2x2pt data vector \mathbf{D} with Models (I) Limber 2x2pt ($w + \gamma_t$, in red), and (IV) 2x2pt non-Limber $w + \text{Limber } \gamma_t$ (in blue). The dashed lines mark the fiducial values. Model (IV) sufficiently removes the large bias in the posterior of n_s in Model (I), and leads to an improvement in the goodness of fit in both the data vector space and the cosmological parameter space (see §5.2.1).

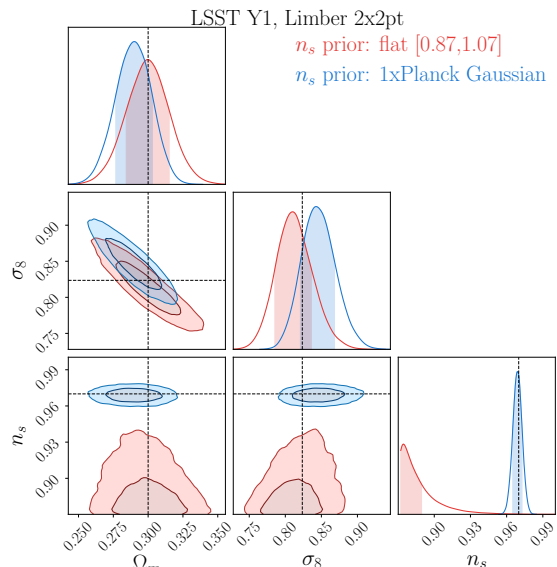


Figure 7. The 1σ and 2σ contours of fitting the LSST Y1 simulated (non-Limber $w + \gamma_t$) 2x2pt data vector \mathbf{D} with Model (I) Limber 2x2pt ($w + \gamma_t$) using the flat prior (in red) and the Gaussian 1xPlanck prior of n_s (in blue). The dashed lines mark the fiducial values. By imposing an informative prior on n_s , the posterior of n_s is pushed back to around the fiducial value, while the other cosmological parameters Ω_m, σ_8 are visibly shifted and especially in Ω_m the 1D bias becomes significant. The goodness of fit is worse in the data vector space with the 1xPlanck prior of n_s , but is better in the cosmological parameter space (see §5.2.2).

6 Discussion and Summary

Extracting precise cosmological information from future photometric galaxy surveys requires improved systematic error control in both observations and models. The Limber approximation, widely used to simplify the computation of the angular power spectra, may become a source of significant errors in the modeling of galaxy clustering and GGL. However, the accurate computation of the angular power spectra, involving double-Bessel integrals, is slow and numerically unstable, unpractical for being incorporated into an MCMC for future cosmological analyses.

We present a new FFTLog-based method to accurately and efficiently calculate the angular power spectra (§2). The new method separates the linear and the nonlinear contributions, the former of which can be factorized into scale and redshift dependent parts, which allows us to reduce the double-Bessel integrals to Hankel transforms and their generalized forms, while the latter can be computed with the Limber approximation. We have also generalized the FFTLog algorithm to deal with integrals with derivatives of Bessel functions (§3), which is present in the RSD contributions and other high-order corrections (e.g., the Doppler effects, see Table 6 of [12] for a list of examples).

Parameters	Fiducial	Prior
Survey		
Ω_{survey}	LSST 12300 deg ² ; DES 5000 deg ²	fixed
σ_e per component	LSST 0.26; DES 0.279	fixed
Cosmology		
Ω_m	0.3	flat [0.1, 0.9]
σ_8	0.82355	flat [0.4, 1.2]
n_s	0.97	flat [0.87, 1.07]
Ω_b	0.048	flat [0.03, 0.07]
h_0	0.69	flat [0.55, 0.91]
w_0	-1	fixed
w_a	0	fixed
$\sum m_\nu$	0	fixed
Galaxy Bias		
b^i	LSST [1.24, 1.36, 1.47, 1.60, 1.76]; DES [1.44, 1.70, 1.70, 2.00, 2.06]	flat [0.8, 3]
Magnification Bias		
b_{mag}^i	LSST [-0.898, -0.659, -0.403, -0.0704, 0.416]; DES [-0.102, -0.102, -0.102, 1.06, 1.06]	flat [-3, 3]
Lens/Source Photo-z		
$\Delta_{z,\text{lens}}^i$	[0, 0, 0, 0, 0];	Gauss (0, 0.005(1 + \bar{z}_{lens}^i));
$\Delta_{z,\text{source}}^i$	[0, 0, 0, 0, 0]	Gauss (0, 0.002(1 + \bar{z}_{src}^i))
Shear Calibration		
m^i	[0, 0, 0, 0, 0]	Gauss (0, 0.005)
IA		
a_{IA}	0.5	flat [-5, 5]
η	0	flat [-5, 5]

Table 1. A list of the parameters characterizing the surveys, cosmology and systematics. The entries are separated by a semi-colon if they are different for LSST Y1 and DES Y6; otherwise, we only write out the shared entry. The fiducial values are used for generating the simulated data vector, and the priors are used in the sampling. Flat priors are described by [minimum, maximum], and Gaussian priors are described by Gauss (μ, σ).

We apply the method to galaxy clustering and galaxy-galaxy lensing (§4), and investigate the impact of the Limber approximation in the context of LSST Y1 and DES Y6 with simulated likelihood analyses (§5). We find that for both surveys, using the Limber approximation to model the 2x2pt correlations results in significant biases in the spectral index n_s . Although Ω_m and σ_8 are less affected in 2x2pt, they are shifted by $\sim 1\sigma$ when the cosmic shear is included (i.e., in the 3x2pt analyses). We then perform the 2x2pt analysis with the non-Limber model of the galaxy clustering and the Limber GGL, and correctly recover the input cosmology, indicating that the non-Limber GGL model may not be needed for these survey analysis choices. Using a non-Limber calculation for clustering only can save a significant amount of computing time and should be considered as an approximation if the error is negligible.

A python version and a C version of the generalized FFTLog code (FFTLog-and-Beyond), are written independently and tested against each other. They are both publicly available at <https://github.com/xfangcosmo/FFTLog-and-beyond>. The code is also incorporated into CosmoLike[30].

Acknowledgments

We thank Jonathan Blazek, Vivian Miranda, Jack Elvin-Poole, Chun-Hao To for helpful discussions. We also thank Rachel Mandelbaum for the updated LSST Y1 source sample distribution, and Oliver Friedrich and Stella Seitz for their distributed notes on bin-averaging and curved sky covariances.

XF, TE are supported by NASA ROSES ATP 16-ATP16-0084 grant. EK is supported by Department of Energy grant DE-SC0020247. Calculations in this paper use High Performance Computing (HPC) resources supported by the University of Arizona TRIF, UITS, and RDI and maintained by the UA Research Technologies department.

A Useful Identities

The Bessel functions and the spherical Bessel functions are related by

$$j_n(z) = \sqrt{\frac{\pi}{2z}} J_{n+1/2}(z). \quad (\text{A.1})$$

The Hankel transform of a power law is given by

$$\int_0^\infty dx x^\alpha J_\mu(x) = 2^\alpha \frac{\Gamma[(\mu + \alpha + 1)/2]}{\Gamma[(\mu - \alpha + 1)/2]}, \quad -1 - \mu < \Re(\alpha) < \frac{1}{2}, \quad (\text{A.2})$$

which has a variant

$$\int_0^\infty dx x^{\alpha-1} j_\ell(x) = \frac{\sqrt{\pi}}{4} 2^\alpha \frac{\Gamma[(\ell + \alpha)/2]}{\Gamma[(3 + \ell - \alpha)/2]}, \quad -\ell < \Re(\alpha) < 2. \quad (\text{A.3})$$

Replacing the Bessel function by its first or second derivative, we have identities

$$\int_0^\infty dx x^{\alpha-1} j'_\ell(x) = -\frac{\sqrt{\pi}}{4} 2^{\alpha-1} (\alpha - 1) \frac{\Gamma(\frac{\ell+\alpha-1}{2})}{\Gamma(\frac{4+\ell-\alpha}{2})}, \quad \left(\begin{array}{l} 0 < \Re(\alpha) < 2, \quad \text{for } \ell = 0 \\ 1 - \ell < \Re(\alpha) < 2, \quad \text{for } \ell \geq 1 \end{array} \right), \quad (\text{A.4})$$

$$\int_0^\infty dx x^{\alpha-1} j''_\ell(x) = \frac{\sqrt{\pi}}{4} 2^{\alpha-2} (\alpha - 1)(\alpha - 2) \frac{\Gamma(\frac{\ell+\alpha-2}{2})}{\Gamma(\frac{5+\ell-\alpha}{2})}, \quad \left(\begin{array}{l} -\ell < \Re(\alpha) < 2, \quad \text{for } \ell = 0, 1 \\ 2 - \ell < \Re(\alpha) < 2, \quad \text{for } \ell \geq 2 \end{array} \right). \quad (\text{A.5})$$

Using mathematical induction, we obtain

$$\int_0^\infty dx x^{\alpha-1} j_\ell^{(n)}(x) = (-1)^n \frac{\sqrt{\pi}}{4} 2^{\alpha-n} \frac{\Gamma(\alpha)}{\Gamma(\alpha - n)} \frac{\Gamma(\frac{\ell+\alpha-n}{2})}{\Gamma(\frac{3+n+\ell-\alpha}{2})}, \quad \left(\begin{array}{l} -\ell < \Re(\alpha) < 2, \quad \text{for } \ell < n \\ n - \ell < \Re(\alpha) < 2, \quad \text{for } \ell \geq n \end{array} \right). \quad (\text{A.6})$$

B FFTLog Versus Brute-Force

We test the galaxy clustering and 5 combinations of GGL power spectra for LSST Y1 in Figure 2 and 3. Here we present the remaining 20 lens-source bin combinations of GGL power spectra for LSST Y1. In Figure 8, on the upper panel in each subplot, we show in solid lines the non-Limber angular power spectra calculated with our FFT method, in dashed lines with the brute-force (BF) quadrature integration. We also plot the Limber result in dash-dotted lines. On the lower panels, we show the fractional differences between the BF and the FFT non-Limber results (BF/FFT-1). The fractional differences are mostly within 1%, with larger errors occurring near the zero-crossing in the power spectra. Larger differences between the Limber and non-Limber results occur when the lens and source bins largely overlap and the overlapping parts of the selection functions are narrow.

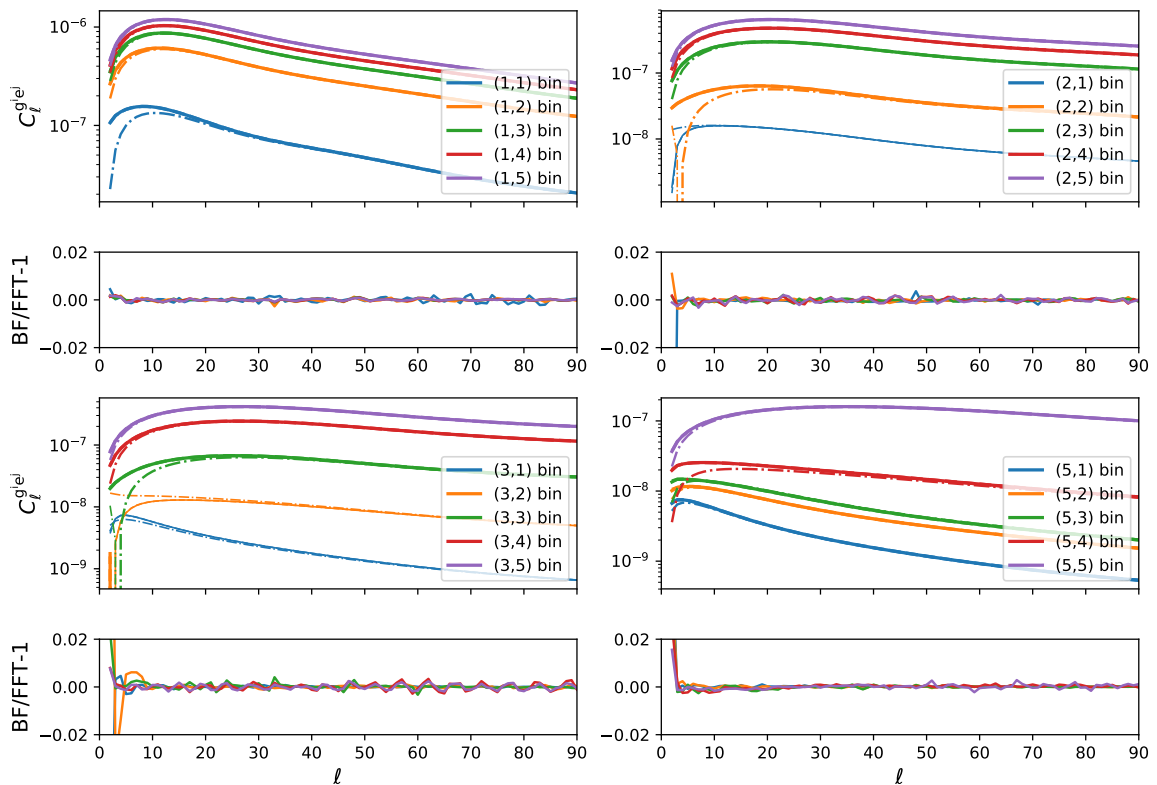


Figure 8. (*Upper panels:*) the remaining 20 lens-source bin combinations of non-Limber GGL power spectra $C_\ell^{g,e}$ in LSST Y1 from the FFT method (solid lines) and the brute-force integration (dashed lines) up to $\ell = 90$, along with the Limber results (dash-dotted lines). The FFT and the BF lines nearly overlap with each other. (*Lower panel:*) fractional differences between the BF and the FFT non-Limber results. The fractional differences are mostly within 1%, consistent with the numerical accuracy of our BF integration. Larger errors occur near the zero-crossing in the power spectra. Larger differences between the Limber and non-Limber results occur when the lens and source bins largely overlap and the overlapping parts of the selection functions are narrow.

References

- [1] The LSST Dark Energy Science Collaboration, R. Mandelbaum, T. Eifler, R. Hložek, T. Collett, E. Gawiser et al., *The LSST Dark Energy Science Collaboration (DESC) Science Requirements Document*, *arXiv e-prints* (Sep, 2018) arXiv:1809.01669, [[1809.01669](#)].
- [2] J. Lesgourgues and T. Tram, *Fast and accurate CMB computations in non-flat FLRW universes*, *J. Cosmol. Astropart. Phys.* **2014** (Sep, 2014) 032, [[1312.2697](#)].
- [3] D. N. Limber, *The Analysis of Counts of the Extragalactic Nebulae in Terms of a Fluctuating Density Field.*, *Astrophys. J.* **117** (Jan., 1953) 134.
- [4] D. N. Limber, *The Analysis of Counts of the Extragalactic Nebulae in Terms of a Fluctuating Density Field. II.*, *Astrophys. J.* **119** (May, 1954) 655.
- [5] P. J. E. Peebles, *Statistical Analysis of Catalogs of Extragalactic Objects. I. Theory*, *Astrophys. J.* **185** (Oct., 1973) 413–440.
- [6] N. Afshordi, Y.-S. Loh and M. A. Strauss, *Cross-correlation of the cosmic microwave*

background with the 2MASS galaxy survey: Signatures of dark energy, hot gas, and point sources, *Phys. Rev. D* **69** (Apr, 2004) 083524, [[astro-ph/0308260](#)].

- [7] N. E. Chisari, D. Alonso, E. Krause, C. D. Leonard, P. Bull, J. Neveu et al., *Core Cosmology Library: Precision Cosmological Predictions for LSST*, *Astrophys. J. Supplement* **242** (May, 2019) 2, [[1812.05995](#)].
- [8] P. Simon, *How accurate is Limber's equation?*, *Astron. Astrophys.* **473** (Oct, 2007) 711–714, [[astro-ph/0609165](#)].
- [9] M. Loverde and N. Afshordi, *Extended Limber approximation*, *Phys. Rev. D* **78** (Dec, 2008) 123506, [[0809.5112](#)].
- [10] V. Assassi, M. Simonović and M. Zaldarriaga, *Efficient evaluation of angular power spectra and bispectra*, *J. Cosmol. Astropart. Phys.* **11** (Nov., 2017) 054, [[1705.05022](#)].
- [11] H. S. Grasshorn Gebhardt and D. Jeong, *Fast and accurate computation of projected two-point functions*, *Phys. Rev. D* **97** (Jan., 2018) 023504, [[1709.02401](#)].
- [12] N. Schöneberg, M. Simonović, J. Lesgourgues and M. Zaldarriaga, *Beyond the traditional Line-of-Sight approach of cosmological angular statistics*, *ArXiv e-prints* (July, 2018) , [[1807.09540](#)].
- [13] M. Schmittfull, Z. Vlah and P. McDonald, *Fast large scale structure perturbation theory using one-dimensional fast Fourier transforms*, *Phys. Rev. D* **93** (May, 2016) 103528, [[1603.04405](#)].
- [14] J. E. McEwen, X. Fang, C. M. Hirata and J. A. Blazek, *FAST-PT: a novel algorithm to calculate convolution integrals in cosmological perturbation theory*, *J. Cosmol. Astropart. Phys.* **9** (Sept., 2016) 015, [[1603.04826](#)].
- [15] X. Fang, J. A. Blazek, J. E. McEwen and C. M. Hirata, *FAST-PT II: an algorithm to calculate convolution integrals of general tensor quantities in cosmological perturbation theory*, *J. Cosmol. Astropart. Phys.* **2** (Feb., 2017) 030, [[1609.05978](#)].
- [16] J. Blazek, N. MacCrann, M. A. Troxel and X. Fang, *Beyond linear galaxy alignments*, *Phys. Rev. D* **100** (Nov, 2019) 103506, [[1708.09247](#)].
- [17] M. Schmittfull and Z. Vlah, *Reducing the two-loop large-scale structure power spectrum to low-dimensional, radial integrals*, *Phys. Rev. D* **94** (Nov, 2016) 103530, [[1609.00349](#)].
- [18] M. Simonović, T. Baldauf, M. Zaldarriaga, J. J. Carrasco and J. A. Kollmeier, *Cosmological perturbation theory using the FFTLog: formalism and connection to QFT loop integrals*, *J. Cosmol. Astropart. Phys.* **4** (Apr., 2018) 030, [[1708.08130](#)].
- [19] Z. Slepian, *On Decoupling the Integrals of Cosmological Perturbation Theory*, *arXiv e-prints* (Dec, 2018) arXiv:1812.02728, [[1812.02728](#)].
- [20] J. E. Campagne, J. Neveu and S. Plaszczynski, *Angpow: a software for the fast computation of accurate tomographic power spectra*, *Astron. Astrophys.* **602** (Jun, 2017) A72, [[1701.03592](#)].
- [21] J. Verner Villumsen, *Clustering of Faint Galaxies: w, Induced by Weak Gravitational Lensing*, *arXiv e-prints* (Dec, 1995) astro-ph/9512001, [[astro-ph/9512001](#)].
- [22] R. Moessner and B. Jain, *Angular cross-correlation of galaxies: a probe of gravitational lensing by large-scale structure*, *Mon. Not. R. Astron. Soc.* **294** (Feb, 1998) L18–L24, [[astro-ph/9709159](#)].
- [23] M. Loverde, L. Hui and E. Gaztañaga, *Lensing corrections to features in the angular two-point correlation function and power spectrum*, *Phys. Rev. D* **77** (Jan, 2008) 023512, [[0708.0031](#)].
- [24] F. Schmidt, E. Rozo, S. Dodelson, L. Hui and E. Sheldon, *Size Bias in Galaxy Surveys*, *Phys. Rev. Lett.* **103** (Jul, 2009) 051301, [[0904.4702](#)].

- [25] J. Liu, Z. Haiman, L. Hui, J. M. Kratochvil and M. May, *Impact of magnification and size bias on the weak lensing power spectrum and peak statistics*, *Phys. Rev. D* **89** (Jan, 2014) 023515, [[1310.7517](#)].
- [26] T. D. Kitching and A. F. Heavens, *Unequal-time correlators for cosmology*, *Phys. Rev. D* **95** (Mar, 2017) 063522, [[1612.00770](#)].
- [27] N. E. Chisari and A. Pontzen, *Unequal time correlators and the Zel'dovich approximation*, *Phys. Rev. D* **100** (Jul, 2019) 023543, [[1905.02078](#)].
- [28] J. D. Talman, *Numerical Fourier and Bessel Transforms in Logarithmic Variables*, *Journal of Computational Physics* **29** (Oct., 1978) 35–48.
- [29] A. J. S. Hamilton, *Uncorrelated modes of the non-linear power spectrum*, *Mon. Not. R. Astron. Soc.* **312** (Feb, 2000) 257–284, [[astro-ph/9905191](#)].
- [30] E. Krause and T. Eifler, *cosmolike - cosmological likelihood analyses for photometric galaxy surveys*, *Mon. Not. R. Astron. Soc.* **470** (Sep, 2017) 2100–2112, [[1601.05779](#)].
- [31] P. Catelan, M. Kamionkowski and R. D. Blandford, *Intrinsic and extrinsic galaxy alignment*, *Mon. Not. R. Astron. Soc.* **320** (Jan, 2001) L7–L13, [[astro-ph/0005470](#)].
- [32] C. M. Hirata and U. Seljak, *Intrinsic alignment-lensing interference as a contaminant of cosmic shear*, *Phys. Rev. D* **70** (Sep, 2004) 063526, [[astro-ph/0406275](#)].
- [33] C. M. Hirata, R. Mandelbaum, M. Ishak, U. Seljak, R. Nichol, K. A. Pimbblet et al., *Intrinsic galaxy alignments from the 2SLAQ and SDSS surveys: luminosity and redshift scalings and implications for weak lensing surveys*, *Mon. Not. R. Astron. Soc.* **381** (Nov, 2007) 1197–1218, [[astro-ph/0701671](#)].
- [34] B. Joachimi, R. Mandelbaum, F. B. Abdalla and S. L. Bridle, *Constraints on intrinsic alignment contamination of weak lensing surveys using the MegaZ-LRG sample*, *Astron. Astrophys.* **527** (Mar, 2011) A26, [[1008.3491](#)].
- [35] M. A. Troxel and M. Ishak, *The intrinsic alignment of galaxies and its impact on weak gravitational lensing in an era of precision cosmology*, *Phys. Rep.* **558** (Feb, 2015) 1–59, [[1407.6990](#)].
- [36] J. Blazek, Z. Vlah and U. Seljak, *Tidal alignment of galaxies*, *J. Cosmol. Astropart. Phys.* **2015** (Aug, 2015) 015, [[1504.02510](#)].
- [37] E. Krause, T. Eifler and J. Blazek, *The impact of intrinsic alignment on current and future cosmic shear surveys*, *Mon. Not. R. Astron. Soc.* **456** (Feb, 2016) 207–222, [[1506.08730](#)].
- [38] H. Hildebrandt, M. Viola, C. Heymans, S. Joudaki, K. Kuijken, C. Blake et al., *KiDS-450: cosmological parameter constraints from tomographic weak gravitational lensing*, *Mon. Not. R. Astron. Soc.* **465** (Feb, 2017) 1454–1498, [[1606.05338](#)].
- [39] S. Bridle and L. King, *Dark energy constraints from cosmic shear power spectra: impact of intrinsic alignments on photometric redshift requirements*, *New Journal of Physics* **9** (Dec, 2007) 444, [[0705.0166](#)].
- [40] M. A. Troxel, N. MacCrann, J. Zuntz, T. F. Eifler, E. Krause, S. Dodelson et al., *Dark Energy Survey Year 1 results: Cosmological constraints from cosmic shear*, *Phys. Rev. D* **98** (Aug, 2018) 043528, [[1708.01538](#)].
- [41] E. Rozo, E. S. Rykoff, A. Abate, C. Bonnett, M. Crocce, C. Davis et al., *redMaGiC: selecting luminous red galaxies from the DES Science Verification data*, *Mon. Not. R. Astron. Soc.* **461** (Sep, 2016) 1431–1450, [[1507.05460](#)].
- [42] J. Elvin-Poole, M. Crocce, A. J. Ross, T. Giannantonio, E. Rozo, E. S. Rykoff et al., *Dark Energy Survey year 1 results: Galaxy clustering for combined probes*, *Phys. Rev. D* **98** (Aug, 2018) 042006, [[1708.01536](#)].

- [43] R. Cawthon, C. Davis, M. Gatti, P. Vielzeuf, J. Elvin-Poole, E. Rozo et al., *Dark Energy Survey Year 1 Results: calibration of redMaGiC redshift distributions in DES and SDSS from cross-correlations*, *Mon. Not. R. Astron. Soc.* **481** (Dec, 2018) 2427–2443, [[1712.07298](#)].
- [44] D. Blas, J. Lesgourgues and T. Tram, *The Cosmic Linear Anisotropy Solving System (CLASS). Part II: Approximation schemes*, *J. Cosmol. Astropart. Phys.* **2011** (Jul, 2011) 034, [[1104.2933](#)].
- [45] R. E. Smith, J. A. Peacock, A. Jenkins, S. D. M. White, C. S. Frenk, F. R. Pearce et al., *Stable clustering, the halo model and non-linear cosmological power spectra*, *Mon. Not. R. Astron. Soc.* **341** (Jun, 2003) 1311–1332, [[astro-ph/0207664](#)].
- [46] A. Stebbins, *Weak Lensing On the Celestial Sphere*, *arXiv e-prints* (Sep, 1996) astro-ph/9609149, [[astro-ph/9609149](#)].
- [47] O. Friedrich, et al., *Dark Energy Survey Year 3 Results: Covariance Methods*, .
- [48] E. Krause, T. F. Eifler, J. Zuntz, O. Friedrich, M. A. Troxel, S. Dodelson et al., *Dark Energy Survey Year 1 Results: Multi-Probe Methodology and Simulated Likelihood Analyses*, *arXiv e-prints* (Jun, 2017) arXiv:1706.09359, [[1706.09359](#)].
- [49] C. Blake and S. Bridle, *Cosmology with photometric redshift surveys*, *Mon. Not. R. Astron. Soc.* **363** (Nov, 2005) 1329–1348, [[astro-ph/0411713](#)].
- [50] C. Wolf, K. Meisenheimer, H. W. Rix, A. Borch, S. Dye and M. Kleinheinrich, *The COMBO-17 survey: Evolution of the galaxy luminosity function from 25 000 galaxies with $0.2 < z < 1.2$* , *Astron. Astrophys.* **401** (Apr, 2003) 73–98, [[astro-ph/0208345](#)].
- [51] B. Joachimi and S. L. Bridle, *Simultaneous measurement of cosmology and intrinsic alignments using joint cosmic shear and galaxy number density correlations*, *Astron. Astrophys.* **523** (Nov, 2010) A1, [[0911.2454](#)].
- [52] P. Schechter, *An analytic expression for the luminosity function for galaxies.*, *Astrophys. J.* **203** (Jan, 1976) 297–306.
- [53] “*NIST Digital Library of Mathematical Functions.*” <http://dlmf.nist.gov/>, Release 1.0.24 of 2019-09-15.
- [54] W. Hu and B. Jain, *Joint galaxy-lensing observables and the dark energy*, *Phys. Rev. D* **70** (Aug, 2004) 043009, [[astro-ph/0312395](#)].
- [55] M. Takada and W. Hu, *Power spectrum super-sample covariance*, *Phys. Rev. D* **87** (Jun, 2013) 123504, [[1302.6994](#)].
- [56] D. Foreman-Mackey, D. W. Hogg, D. Lang and J. Goodman, *emcee: The MCMC Hammer*, *Publ. Astron. Soc. Pac.* **125** (Mar, 2013) 306, [[1202.3665](#)].
- [57] Planck Collaboration, N. Aghanim, Y. Akrami, M. Ashdown, J. Aumont, C. Baccigalupi et al., *Planck 2018 results. VI. Cosmological parameters*, *arXiv e-prints* (Jul, 2018) arXiv:1807.06209, [[1807.06209](#)].